THERMAL INFRARED WEATHERING TRAJECTORIES IN HAWAIIAN BASALTS: RESULTS FROM AIRBORNE, FIELD AND LABORATORY OBSERVATIONS

A THESIS SUBMITTED TO THE GRADUATE DIVISION OF THE UNIVERSITY OF HAWAI'I IN PARTIAL FULFILLMENT OF THE REQUIREMENTS FOR THE DEGREE OF

MASTER OF SCIENCE

IN

GEOLOGY AND GEOPHYSICS

AUGUST 2006

By
Orion Carlisle

Thesis Committee:

Paul Lucey, Chairperson
Scott Rowland
Jeff Taylor

We certify that we have read this thesis and that, in our opinion, it is satisfactory in scope and quality as a thesis for the degree of Master of Science in Geology and Geophysics.

THESIS COMMITTEE

Chairperson

ACKNOWLEDGMENTS

I would like to thank Sarah Sherman for all her wonderful help and guidance in the field and lab. I would also like to thank Keith Horton for his help with the D&P.

TABLE OF CONTENTS

LIST OF TABLES

LIST OF FIGURES

CHAPTER 1
INTRODUCTION

Basalts are ubiquitous in the inner solar system. They are known to occur on the Moon, some asteroids (particularly Vesta), Mars and seventy percent of the surface of the Earth. A small fraction of Earth's basalts are exposed subaerially on high oceanic volcanoes including Hawaii, the Canaries and the Galapagos. Remote sensing studies of these volcanoes must include an understanding of the effect of weathering on their surface physical and chemical properties. Such an understanding is, to some extent, even relevant to studies of basalts on Mars that may have been weathered by processes analogous to those that occur on high oceanic islands.

The range of weathering zones and ages of basaltic lava flows on the Island of Hawaii make that locale ideal for the study of basaltic weathering. This was recognized by *Farr and Adams* [1984] and *Kahle et al.* [1988] who conducted field, laboratory and remote sensing studies of basaltic lava flows of Mauna Loa volcano. These studies found systematic relationships among physical properties, spectral properties, ages and environmental conditions of individual flows.

Since that pioneering work, substantial progress in the technology of remote sensing and field spectral measurement has occurred. In this thesis I revisit the study area of *Kahle, et al.* [1988], and use these new methods to confirm the earlier studies and to extend them. I obtained both field spectroscopic and remote sensing data of similar quality to those obtainable in the laboratory, allowing the effects of disturbance by sampling to be controlled, and to assess the variability of spectral properties within flows. The spectral work is supported by sample analysis of the elemental properties of samples collected from the sites to understand the controls on the observed spectral behavior. I confirm the results of the earlier studies, and show that no new insights are available from my new data; however, the confidence in the earlier results is substantially improved by my more comprehensive and controlled study.

Background

Farr and Adams [1984] studied rock coatings that form on Hawaiian lava flows and the influence of climate ranges in which the coatings form. They concluded that where rainfall is less than about 125cm/yr, the weathering of rock surfaces is dominated by mechanical spalling and formation of surface coatings; where rainfall is greater than 125cm/yr, lichen

growth dominates [*Farr and Adams*, 1984]. On Mauna Loa, the coatings progress from thin clear coatings of clear hydrous silica layers with small amounts of aluminum, to thicker coatings incorporating various amounts of dust particles, which seem to be locally-derived oxidized basaltic detritus [*Farr and Adams*, 1984]. *Elvidge* [1979] indicated that desert varnish may form where rainfall is less than about 25 cm/yr. *Farr and Adams* [1984] described coatings on a sample from Kohala (where precipitation is less than 25 cm/yr) as being similar to desert varnish.

Kahle et al. [1988] used an observed correlation between TIR spectral features and age to map flows on Hawaii using data from the Thermal Infrared Multispectral Scanner (TIMS). Figure 1 and Figure 2 show locations of sample sites of their study. TIMS has six spectral channels between 8 and 11.7μm, with spectral widths between 0.4 and 0.8μm. The maps were created by performing a decorrelation stretch on TIMS channels 1, 3 and 5. The decorrelation stretch highlights spectral variances and results in three variance bands [*Alley*, 1996; *Gillespie, et al.*, 1986]. Kahle et al. combined these variance bands into false color images (Figure 3). They concluded that age-related changes in TIR spectral features were caused by differences in the weathering state, such as the preservation and alteration of glassy crusts, the oxidation of iron, and the accretion of silica-rich coatings [*Kahle, et al.*, 1988].

They identified three primary features in laboratory TIR hyperspectral data of pahoehoe samples (labeled A, B and C in Figure 4): two narrow features at ~8.2μm (Feature A) and ~9.2μm (Feature B) and a broad feature centered at ~10.5μm (Feature C). Feature A, when it existed, appeared as a hump on the feature B. Due to low spectral resolution, only feature B could easily be identified in TIMS data (Figure 5). The other two features could only be inferred in TIMS data from an overall depression in values at the short and long wavelength ends of the spectral range. Aa flow samples also contained these three features; however, the features' strength was reduced. The C feature was especial hard to identify in aa spectra. In the pahoehoe samples, *Kahle et al.* [1988] observed that the position of feature B shifted to lower wavelengths (~9.2 to 9.1μm) for spectra with a prominent feature A. However, since this shift was less than TIMS spectral resolution, they did not pursue this any further. They concluded that the mapping technique is best used on sparsely vegetated flows less than 1.5ka in age [*Kahle, et al.*, 1988]. Other studies showed that the older flows are mapped better using the near-IR and visible spectral regions [*Abrams, et al.*, 1991; *Kahle, et al.*, 1988].

CHAPTER 2
EXPERIMENTAL APPROACH

As mentioned in the introduction, the intent of this thesis is to attempt to duplicate, confirm if possible, test and extend the results of previous work. The approach is to integrate field, remote sensing and laboratory analyses to arrive at a qualitative model of basaltic weathering under the conditions that prevail at the Mauna Loa study site. The laboratory analyses will enable correlation of spectral properties with physical and chemical properties of the surfaces of samples returned from the site; field spectroscopic measurements will establish whether the sampling has disturbed the optical surface, and remote sensing will establish whether the spectral properties previously observed are representative of the flows under study.

Field Area

The study area (Figure 6) is located in the saddle between Mauna Loa and Mauna Kea along the Northern flank of Mauna Loa. It is enclosed within a box [19°37'25"N 155°35'15"W] [19°38'20"N 155°28'20"W] [19°38'5"N 155°28'20"W] [19°37'10"N 155°35'15"W], which runs roughly parallel to the old Hilo-Kona Road (also known as the Hilo-Kona Jeep Trail). The ground elevation ranges from 2000-2300 meters generally decreasing from west to east. Precipitation grades from 50 to 130 centimeters/year (west to east) along the study area [*Armstrong*, 1983]. Field observations indicate that the area is generally low in vegetation, though older flows tend to have more growth. Vegetation primarily consists of lichen, bushes and trees. The study area includes seven age groups of lava flows ranging from 0.07ka (ka=thousand years ago) to flows older than 8ka, grouped after *Kahle et al.* [1988]. The ages for prehistoric flows were derived from radiocarbon dating of charcoal extracted from beneath the flows, with some dates coming from *Rubin et al.* [1987], and other coming from Lockwood (unpublished data referenced in *Kahle et al.* [1988]). I chose ten sample sites within this area. See Table 1 for site name, flow age, and brief description. See Figure 7 and Figure 8 for photos of the study area. The reasons for selecting this area are:

- It allowed for comparison to past studies such as *Kahle et al.* [1988], *Abrams et al.* [1991], and *Farr and Adams* [1984].
- It includes a wide range of flow ages that are easily accessible for sampling and imaging. Seven age groups spanning from 1935AD to over 8ka.

- The annual rainfall is within the preferred range as discussed by *Kahle et al.* [1988], *Farr and Adams* [1984], *Elvidge* [1979]. [25cm/yr – 125cm/yr]; enough precipitation to prevent desert varnish [*Elvidge*, 1979; *Kahle, et al.*, 1988], but not enough to promote rapid lichen growth [*Farr and Adams*, 1984; *Kahle, et al.*, 1988].

A second area, located on Kilauea on the down hill side of the Pulama Pali was included to include the characteristics of fresh pahoehoe. Because the samples collected here were only a few hours to a few days old (labeled as 0ka) and the weather at that time had been dry, precipitation rates for these samples are not an issue. Because Mauna Loa and Kilauea basalts are petrologically similar [*Kahle, et al.*, 1988; *Wright*, 1971], the Kilauea pahoehoe should be a reasonable proxy to the non-existent fresh pahoehoe from Mauna Loa.

Samples

Rock samples were collected from the Mauna Loa study area along the old Hilo-Kona road on August 28, 2003. Fresh rock samples (a few hours to a few days old) were collected from Kilauea near the ocean terminus of an active flow, on August 29, 2003. Additional samples were collected May 20-23, 2005 along the old Hilo-Kona Road. Digital photos were taken at time of collection, which included context photos of the surrounding flow and close up photos of each sample. Some samples were divided into splits for microprobe analysis. Figure 6 shows the sampling locations within the study area. Figure 9 shows the sampling locations relative to the remote sensing data described below.

Microprobe

The spectral properties observed are reflections of the chemical and mineralogic composition of the optical surface of the exposed flow surfaces. Based on the earlier studies [*Farr and Adams*, 1984; *Kahle, et al.*, 1988; *Kraft, et al.*, 2003], silica coatings and phyllosilicates are important, so we chose to measure Al, Si, Fe, Mg, and Ca. To characterize the surfaces I had thin sections made of some of the samples. The intent was to microprobe across the surface of the sample to determine the thickness and composition of any coating. Since the surface coating might be fragile and come off during the thin-section-making process, the samples were dipped in epoxy to strengthen the surface. Microprobe mineral map data were collected on a 1992 CAMECA SX50 Electron Microprobe with 5

wavelength-dispersive spectrometers using SAMx software and the help of Dr. Kent Ross. The microprobe was calibrated using a laboratory standard prior to each run. Data were collected for Al, Si, Fe, Mg, and Ca at a spatial resolution of 10μm per pixel.

Laboratory Reflectance

Laboratory spectra are necessary to link the physical and chemical measurements conducted on the samples to the field and airborne spectroscopy. The laboratory spectra were collected under controlled conditions with a Thermo Nicolet NEXUS 470 FT-IR spectrometer using a gold integrating sphere and a liquid-nitrogen-cooled MCT detector [*Hamilton and Lucey*, 2005]. The spot size (the area observable by the spectrometer) was 25mm in diameter, and the system was configured to collect 100 scans that were co-added for each sample. The spectrometer was set up with a spectral range of 5 to 17μm with a spectral resolution of 0.01 to 0.11μm. For the range of 7 to 12μm the spectral resolution is 0.03 to 0.06μm. The sample spectra were ratioed to the spectrum of a diffuse gold plate used as a reference. To reduce spectral contributions from water vapor, dry air was continuously pumped through the spectrometer and sample chamber, and a 15-minute purge was conducted after sample placement before recording data. The reflectance spectra were converted to apparent emissivity using Kirchhoff's law $\varepsilon=1-R$ where ε=emissivity and R=reflectance [*Hunt*, 1980; *Kahle, et al.*, 1988; *Salisbury and Walter*, 1989].

Thermal Infrared Field Spectroscopy

To obtain high quality spectra of the flows without disturbing the surface, and to provide ground truth for the airborne data, we also sampled the study area with a portable emittance FTIR spectrometer. Figure 6 and Figure 9 show the locations of the field spectral measurements. Figure 10 shows the spectrometer in the field. The field measurements were taken with the Designs and Prototype Model 101 μFTIR field spectrometer (D&P) [*Gillespie, et al.*, 1996; *Korb, et al.*, 1996]. The D&P is sensitive over a spectral range of 3-14μm, although for this study only the range covering the airborne remote sensing spectral range was used (7 to 12μm). Signal to noise ratios of the spectra were improved by co-adding 16 scans. In the field, the D&P was set up on a tripod at a height of ~1 meter with the optics pointed out ~40 degrees from vertical. This gave a field of view of about 7cm. Two surface radiance readings were taken on different 7cm spots at each site. Downwelling radiance correction and absolute emissivity were obtained following procedures outlined by *Horton et al.* [1998] (See Appendix A). A temperature adjustable

blackbody was attached to the optics to collect calibration data. The temperature was set to ~10°C below and ~10°C above the sample temperature. The ground temperature was measured with an OMEGASCOPE® Handheld Infrared Thermometer with emissivity set at 1. To correct for downwelling radiance, we collected spectra from the diffuse side of crinkled aluminum foil for each surface measurement taken. See Appendix A for a description of the downwelling-radiance-correction method.

Airborne Thermal Infrared Data

This study used the University of Hawaii's Airborne Hyperspectral Imager (AHI), which has 256 bands covering 7 to 11.5μm [*Lucey, et al.*, 1998]. See Appendix B for description of the AHI system. AHI also collects GPS and orientation data to enable georeferencing. The study area was traversed with three flight lines flown parallel to the old Hilo-Kona road near the top of the Mauna Loa-Mauna Kea saddle on the island of Hawaii (Figure 6). Due to the relatively rapid calibration degradation (see Appendix B), each strip was split into two runs, each about 6 km in length and requiring about two minutes to complete. Black body calibration measurements were collected before and after each run. Data collection took place between 9 and 10 a.m. local time. Weather conditions in the study area were optimal, with no clouds and minimal air disturbance. The plane was flown at ~145 knots at an altitude between 3400 and 3550 meters. The elevation of the ground ranged from 2000 to 2300 meters giving a height above ground ranging from 1100 to 1550 meters. This gave a range of swath widths from 135-190 m, and a cross track spatial resolution of ~0.5-0.7 m/px.

Calibration of AHI data is described in *Winter et al.* [2004]. Four blackbody spectra (collected at temperatures of 15, 20, 25 and 30°C) were collected immediately before each run (pre-BB), and five blackbody spectra (15, 20, 25, 30 and 35°C) were collected immediately after each run (post-BB). These blackbody spectra were used to calibrate the raw data and give radiance spectra in $W/m^2/\mu m/sr * 1000$. Run-3 post-BB 25, 30 and 35°C spectra were corrupted and not used in the processing. See Appendix B for more information on the calibration process.

Only spectral channels 25-205 (7.9-11.4μm) were used because the rest of the channels showed low signal to noise ratios. Two types of processing were run on these data; Principal Component Analysis (PCA) to aid in the production of false color images of the lava

flows for comparison to TIMS data, and emissivity extraction (described in Appendix C to produce emissivity spectra that can be compared to laboratory and field (ground truth) spectra.

CHAPTER 3
RESULTS

Samples

Overall, the visual appearances of the samples' surfaces vary with age from dark-glassy-blackish in the younger samples to light-dull-reddish in the older samples (Figure 11). Starting with the youngest samples, 0ka pahoehoe has a glassy surface that has a yellow/blue/purple metallic luster overriding a black background. This glassy surface immediately begins to spall, revealing a rougher glassy interior as in the ML1935 flows (0.07ka). This rough glassy surface then begins to weather, becoming duller and redder and lighter. The surface also begins to smooth out with age, possibly a combination of chemical and physical weathering, filling of the vesicles with debris (in situ and foreign), and the formation of coatings. Table 1 gives a summary of sample descriptions for each flow group. A key observation is that there is a discontinuity in visual weathering trend for the 0.2-0.5ka flow. There are two branches of this flow within the study area, one on the west (dry) end and one on the east (wet) end. The western branch looks like the younger flows; mostly black with some luster remaining, with little to no vegetation. The eastern branch resembles the 1.5-4ka flow; the surface is a dull, reddish-gray color and bushes are scattered around.

Thin Section Analysis

The electron microprobe was used to generate mineral maps of thin sections cut from rock surfaces as described in the methods section. Silica rich coatings or phyllosilicate alteration products are easily detected by measuring Si, Al and Fe and displaying a map assigning Si to red, Al to green, and Fe to blue. Plagioclase thus shows up as yellow, pyroxene as magenta, olivine as purple and the glass matrix as a pale yellow (Figure 12). The silica coatings, which include some aluminum, show up as orange.

The younger Mauna Loa samples do not show any signs of surface coatings. However, the older samples have a Si-Al rich coating that increases in thickness with age (Figure 13). Furthermore, a material consisting of Si and Fe (though other elements not measured for may be present) fills the vesicles near the surface. This may be important to the TIR

signature. Loose material on the surface may have been lost during thin section preparation. Significant amounts of loose, material could contribute significantly to the airborne TIR spectra.

In the few hours old pahoehoe sample there are numerous small (~150-250μm) crystals of plagioclase and pyroxene. There are also a few crystals of olivine, most of which are small (~150μm), but some phenocrysts are medium sized (~500-750μm). Along the surface there is no sign of coatings. The sample is essentially uniform from surface inward (1cm), with the exception of the olivine crystals that are larger the further into the sample they are.

In the 0.07ka sample there are numerous small (~50-250μm) crystals of plagioclase, pyroxene and olivine. Along the surface there is no sign of coatings. The sample is essentially uniform in the outer 1 cm.

The 0.16ka sample has numerous small (~150-250μm) crystals of plagioclase. There are small (100-250μm) and medium (500-700μm) sized crystals of pyroxene. There are also a few crystals of olivine, most of which are small (50-100μm), but some are medium sized (~500). There is a silica coating with an average thickness less than 10μm.

The 0.2-0.5ka has numerous small (~50-250μm), and medium (500-700μm) crystals of plagioclase and pyroxene. There are also a few crystals of olivine, most of which are small (~100μm), but some are medium sized (~300-600μm). There is a silica coating with an average thickness of around 14μm.

The 1.5-4ka sample has numerous small (~150-250μm) crystals of plagioclase. There are some small (50-250μm) and medium (~500) sized crystals of pyroxene. There are some small (~250μm) and some large (~1000μm) crystals of olivine. Many of the olivine crystals are elongated. There is a silica coating with an average thickness of 47μm.

The 4-8ka sample consists mainly of large (1000-2000μm) olivine phenocrysts in a glass matrix with one large pyroxene crystal and no signs of plagioclase. There is a Si-Al surface coating with an average thickness of about 31μm. There are a couple of coating protrusions that have diameters of 120 and 136 ± 5μm.

Laboratory Reflectance

For laboratory, field and remote spectra, feature locations were determined by fitting Gaussian curves to the spectra (Figure 14). The center of each fitted Gaussian curve is taken as the feature location. The Gaussian depth was used as feature depth.

Three features are observed at 8.2μm (feature A), 9.2μm (feature B) and 10.9μm (feature C) which correspond to the features discussed by Kahle et al. [1988]; see Figure 15. Only features A and B exhibit a correlation between peak intensity and flow age. Feature C is dominant in the 0ka pahoehoe. Feature B also exists in the 0ka pahoehoe spectra, but its intensity varies greatly among the 0ka pahoehoe samples, from a mere shoulder on feature C to a well established peak equal in prominence to feature C, although not as broad. There is no feature A in the 0ka pahoehoe samples.

In the 0.07ka samples, feature C has almost faded into the background and feature B is well established as the main feature. Feature A also becomes apparent at this time as a narrow shoulder on feature B. Feature A grows and shrinks along with the B feature, but always remains smaller. Both features increase in strength up to the 0.2-0.5ka (western branch) sample, but then decrease steadily to the >8ka sample. An exception to this growth and decay trend is the 0.2-0.5ka flow. While the emissivity spectrum of the sample from the western branch of the 0.2-0.5ka flow fits into the trends just described, the sample from the eastern branch has an emissivity spectrum similar to the sample from the older 0.5-1.5ka flow.

Figure 16 shows plots of age trends for the A and B features in the laboratory data. There is no trend between feature A position and age. However there is a trend for feature B position vs. age. The B feature initially shifts from 9.18μm (0ka) down to 9.12μm (0.2-0.5ka). Then it shifts upward to 9.38μm in the >8ka flow. The B feature position is also correlated with the A feature strength. The 0.07ka flow has a weak feature A, and feature B is centered at 9.18μm. In the 0.16ka and 0.2-0.5ka flow, feature A becomes prominent as feature B shifts down to ~9.12μm. In the 1.5-4ka and 4-8ka flows, the whole spectrum has become flatter, but the B feature is still readily identifiable, and has shifted up to 9.23μm.

Thermal Infrared Field Spectroscopy

Emissivity spectra taken with the D&P at the field sites closely match the apparent emissivities obtained from laboratory reflectance spectra of samples collected from the same flows. Figure 15 shows the absolute emissivity of the eight sample areas. There are

two obvious features; one at about 8.2μm (A), and another at about 9.2μm (B). The spectra show a sharp increase in the B Feature depth with age from 0.07ka to the 0.2-0.5ka flow; then a sharp decrease at the 0.5-1.5ka flow, followed by a steady decrease to the oldest sample (Figure 17). The weaker A feature, appearing as a hump on the B feature, follows a similar trend. The only deviation from this trend is in the 0.2-0.5ka unit. While the western branch of the 0.2-0.5ka flow fits into the trends just described, the emissivity spectrum of the eastern branch would fit in better between the older 0.5-1.5ka and 1.5-4ka flows. There is a correlation between B feature position and age with position increasing with age. There is no correlation between feature position and age for the A feature.

Airborne Thermal Infrared Data

Spectral Results

The most obvious feature in the relative emissivity plots of the AHI data (Figure 15) is the B feature at ~9.13μm. This feature grows with flow age until 0.2-0.5ka (western branch), then decreases with age, vanishing by >8ka. Again, the notable exception to this trend is in the 0.2-0.5ka flow, where the western branch fits into the age trend just discussed, but the eastern branch resembles the older 1.5-4ka flow. A second features at around 8.1μm (feature A) exists as a shoulder on the B feature. Its strength follows a similar age trend as the B feature. However, as the A and B feature strengths decrease, the B feature decreases faster and the contrast between the two features decreases. Except for a slight initial increase in position, the position of the 9.2μm feature shifts to longer wavelengths with age (Figure 18). There was no correlation between the 8.2μm feature position and flow age. However, it does exhibit the initial shift to lower wavelength before leveling off. There is a third feature at around 11μm (C feature) evident only in the 0.07ka flow.

Uniformity of Sample Areas

An important role of the remote sensing is to show how representative the sampling sites are of the whole flow. A sensitive method for discerning differences among spectral units is principal components analysis, relied upon heavily by *Kahle et al.* [1988] in their study. In TIR spectrometry, the bands tend to be highly correlated [*Private discussion with Paul Lucy*, 2005]. The spatial variations in spectral properties are subtle, and tend to be overridden by strong temperature variations. Principal Component Analysis (PCA) is a

mathematical procedure used to view variation within a data set that has more data points than variables. The outputs are uncorrelated PC bands; each contains information on some variation within the data set. For TIR, the first PC band (PC1) tends to be highly correlated to temperature. The second PC band (PC2) usually is correlated to differences in the major spectral band (i.e. the silicate feature around 9.1μm). PC2 may also be associated with the amount of vegetation (if present). The remaining PC bands will show subtle variations in band shape, such as relative depths of the three bands identified in the lab spectra. To create the flow maps, I used the first three PC bands, assigning PC1 to red, PC2 to green, and PC3 to blue. The resulting image has been georectified (Figure 9).

There is a color shift with age. The color starts off as red-orange in the 0.07ka flow, and then shifts to purple in the 0.16ka flow. The color then shifts to a dark pink in the 0.5-1.4ka flow; and a light pink by the 4-8ka flow. The >8ka flow shows up as green; very similar in color to the aa flows. An interesting exception is with the 0.2-0.5ka flow. The western branch of the 0.2-0.5ka flow shows up as a purple (with some pink) which fits into the color trend just described. However the eastern branch more closely resembles the older 1.5-4ka flow in color. Near the sample sites the sampled regions are similar in color; hence spectra properties should be the same. This indicates the samples should be representative of their respective flow within the study area.

CHAPTER 4
DISCUSSION

Remote sensing, laboratory and field spectra all show age related trends. The C feature is strong in the 0ka flow. It is barely observable in latter flows and is gone completely by the 0.5-1.5ka flow. The A and B features initially increase with age to 0.2-0.5ka; they then decrease with age, at first quickly then more slowly. The exception to this is the 0.2-0.5ka flow. The spectra of the western branch of the 0.2-0.5ka flow fit into the trend just described, but the spectra of the eastern branch look more like the spectra of the older 0.5-1.5 or 1.5-4ka flows. Field observations also show this discontinuity. The eastern branch of the 0.2-0.5ka flow shares a similar appearance to the 1.5-4ka flow with established vegetation and the red hue of iron oxidation. The western branch of the 0.2-0.5ka flow is mostly free of vegetation and is still dark and vitreous, similar to the younger 0.16ka flow. The main environmental difference between the two branches of the 0.2-0.5ka flow is annual precipitation. The eastern branch has a precipitation rate of 127 cm/yr; the western branch precipitation rate is 89 cm/yr [*Armstrong*, 1983].

Microprobe data indicates a weak age-related trend in the formation and growth of a silica coating on the rocks. This coating is not measurable in the 0ka and 0.07ka samples. It is first observed in the 0.16ka sample and increases with age to become the thickest on the 1.5-4ka sample, and then decreases on the 4-8ka sample. Meanwhile the A and B features increase with age to 0.2-0.5ka and then decrease with age thereafter. The coating thickness and A and B feature depths are thus only partly correlated. Also notable is that even though the 0.2-0.5ka sample used for microprobe work was from the eastern branch, it is significantly thinner than the coating on the 1.5-4ka sample. The similarity of visual observations and spectra of these sites does not translate into similarity in the silica coating thickness. Also there is neither a trend in feature position or strength with coating thickness (Figure 19).

Origins of spectral features

It has been proposed that silica coatings are responsible for the B feature and possibly the A feature [*Kahle, et al.*, 1988]. However, if this is the case, it seems that it would only be responsible for the existence of the features and not the feature depths. The B feature is not a reststrahlen band of olivine, pyroxene, or plagioclase (the typical phenocrysts of

Hawaiian basaltic rock), nor is it due to the weathering products magnetite and ilmenite. Additionally the peak is too narrow to be a result of the amorphous glass matrix [*Kahle, et al.*, 1988].

According to Crisp et al. [1990], based on comparisons to spectra of synthetic glasses, most peaks in samples taken from the same area as this study could be attributed to vibrations in glass structures. Crisp et al. explains this as being due to polymerization of glass. In their study of young basalts (1855 AD and younger), they found that the spectra of fresh (0ka) Hawaiian basalts exhibit a single broad feature centered around 10.3-10.5μm. With age, this feature splits into two features at 9.2-9.25μm and 10.5-10.8μm. These features correspond to the B and C features in my study. Also with age, the B feature was found to shift down to 9.1-9.15μm and the C feature shifted up to 10.7-10.9μm. The C feature starts off the strongest but is then is gradually replaced in prominence by the B feature. This, Crisp et al. explain, would be consistent with increasing polymerization of the glass surface. First the glass polymerizes into mostly chainlike units (Feature C) and some sheetlike units (Feature B). Over time the polymerization tends to favor the sheetlike units, increasing B and reducing C. Polymerization also causes the B feature to shift to shorter wavelengths and the C feature to shift to longer wavelengths [*Mysen*, 1983]. Also "...Fe^{3+} is considered a network former and Fe^{2+} is considered to be a network modifier..." [*Crisp, et al.*, 1990]; therefore, iron oxidation may reduce the C feature and enhance the B feature as well.

Coating

Kraft et al. [2003] published a study of the effects of silica coatings on TIR spectra of basaltic rocks. They applied fine mists of colloidal SiO_2 to polished slabs of Columbia River Basalt (CRB), and allowed the solution to evaporate and thereby precipitate silica. The polished slabs of CRB represent unweathered basaltic glass. By repeating this process they produced amorphous silica layers of differing thicknesses. They then recorded thermal emission spectra of the prepared samples. They compared thermal emission spectra w/coating thicknesses ranging from 0μm (uncoated CRB) to 6.3μm. (Figure 20). As the thickness of the amorphous silica layer increases, the broad peak centered near 10μm (the basaltic contribution) diminishes and is replaced by a strong peak at ~9μm and an accompanying shoulder at ~8μm (the 9 and 8μm peaks representing the amorphous silica contribution) [*Kraft, et al.*, 2003]. These peaks correspond to B and A features respectively.

So as a silica coating gets thicker, the A and B features should get stronger until the coating is about 10μm, and remain constant thereafter. What I am seeing in my study is that this is initially the case. The coating gets thicker as the A and B spectral features increase in strength and the C feature diminishes. But then the A and B features begin to decrease even as the average thickness of the coating is still increasing. The study by *Kraft et al.* [2003] was done under controlled conditions producing even and uncontaminated coatings. In contrast, my samples come from uncontrolled conditions; the coatings are not uniform, and they incorporate other matter which can reduce contrast. The nonuniformity of coating thickness seems to be greater with increased coating thickness which may help explain the reduced spectral contrast with age in later flows.

A study by *Curtiss et al.* [1985] indicates that silica coatings can be formed from the leaching of dust or tephra. Dust is first deposited on the surface of the rock. A low impact wetting event such as dew or fog allows for the leaching of silica and salts from the dust grains without washing them away. A drying period precipitates silica onto the rock. A high impact wetting event such as heavy rain, washes away the salts and other leftover products from the surface. The cycle is repeated as more dust is deposited on the surface. Heavy wetting events not only end up washing away the sources, but also disrupt silica matrix formation [*Curtiss, et al.*, 1985].

This would help explain the poor correlation between annual precipitation and silica coating thickness. The precipitation amounts reported are yearly totals and do not discriminate between types of precipitation [*Armstrong*, 1983]. Nor do such statistics indicate how long water/moisture is left standing on the rock surface. A study published by *Juvik and Perreiera* [1973] shows that fog contributes up to 33% of the precipitation measured over a 28 week period, and the amount and percentage of fog varied with altitude. However, there were only 4 stations with only one near my study area. I propose that within the study area, all flows are exposed to similar amounts of low impact wetting events, thus allowing for similar rates in silica coating formation. The main difference in annual precipitation would come not from low impact wetting events but from the heavier impact events. It is these events that result in the different rates of weathering between east and west most flows of the 0.2-0.5ka unit.

An integrated picture of the evolution of basaltic pahoehoe surfaces emerges: Fresh lava (a few days old) exhibits a smooth glassy chill coat that spalls quickly to reveal a glassy vesicular surface. Both surfaces are responsible for a single broad TIR feature

around 10.5μm. As glass begins to polymerize, this feature splits into a 9.2μm and a 10.7μm feature with the 9.2μm increasing in strength and the 10.7μm feature diminishing with further polymerization (these features correspond to the B and C features discussed earlier), Meanwhile, an amorphous silica coating forms from the leaching of tephra and/or detritis. This coating gives rise to two features (one at 8.2μm and another at 9.2μm) while masking the C feature of the basaltic glass. The 8.2μm corresponds to the A feature, and the 9.2μm, combining with and ultimately masking the similar feature of the basaltic glass, corresponds to the B feature. As the coating thickens, the C feature is diminished, disappearing altogether at a coating thickness of about 10μm (though this is variable depending on overall coverage of the coating). As time continues, the competing process of weathering degrades the surface faster than the silica coating forms, resulting in the reduction of feature strength.

The maps of lava flows using the hyperspectral data of AHI produce qualitatively similar results to those produced by Kahle et al. [1988] using three channels of TIMS' data. The pahoehoe flows are readily identified from the aa flows and from each other. The aa, though differentiated from the pahoehoe, appear very similar to each other, the >8ka pahoehoe flow, and vegetation. This lack of differentiation of the aa is due mostly to cavity radiation which reduces spectral contrast. The use of hyperspectral vs. multispectral data does not seem to have produced any new information in regards to mapping. However, the correlation between the B feature position and age is measurable in the AHI data. It was not measurable in the TIMS data.

CHAPTER 5
CONCLUSION

This study has both confirmed and extended previous work. Our PCT map using AHI data is qualitatively similar to *Kahle, et al.*'s [1988] PCT maps made with TIMS data. Furthermore, we find similar age related trends between our laboratory data and *Kahle, et al.*'s [1988] laboratory data. Using the AHI, we are able to observe age related trends similar to those in the laboratory and field data, indicating that the sampling used for the lab and field data are representative of respective field sites. The similarity between laboratory data and field data indicate that sample gathering has little if any effect on TIR spectral properties of the surface.

We also find that coating thickness and spectral property trends are not matched. The silica coating thickness varies only with age, whereas various the spectral properties not only vary with age, but also seem to vary with annual precipitation. The silica coating gives rise to the A and B features which initially increase in strength with age. But other weathering processes, possibly associated with heavy wetting events, ultimately win out, and begin to reduce the strengths of the spectral features and lower the spectral contrast.

Various weathering processes are taking place on the pahoehoe surfaces: spalling, oxidation, coating formation, vegetation growth, and mechanical. Spalling takes place soon after emplacement. The others are ongoing and cumulative processes. Silica coating formation proceeds rapidly at first then trails off. Although oxidation and vegetation seem to follow an age-related trend, there is a discontinuity when two flows of the same age receive different amounts of annual precipitation. The flow receiving more precipitation weathers faster. The TIR spectra show an age-related trend that is also influenced by annual precipitation. Although it has been proposed in the past that the growth of a silica coating was responsible for the A and B features, there is an incongruity. Initially the features increase in strength with increasing silica coating thickness, but they then begin to decrease even though the coating continues to grow. Furthermore, the spectra of eastern branch of the 0.2-0.5ka flow resemble that of older flows, but the silica coating does not. Perhaps the differences are due to the different contribution of light wetting events (i.e. fog or mist) versus heavy wetting events (i.e. rain). The flows in the study area maybe receiving similar amounts of fog which facilitates silica coating growth. However, some parts may receive significantly more rain, which causes their surfaces to weather faster, disrupting the silica coating.

More attention needs to be focused on the competing processes of amorphous silica coat formation and other weathering events, especially the role different wetting events play in the processes. That is, how do heavy rain, light rain, fog and dew affect the surfaces? In trying to explain the spectral features over time, more than just annual precipitation values need to be taken into consideration. We also need to consider the types and duration of precipitation events.

APPENDIX A
CORRECTION OF FIELD SPECTROSCOPIC DATA

The downwelling radiance correction was obtained by following procedures outlined by Horton et al. [1998] Roughened aluminium foil was used in lieu of a diffuse gold plate. The two surfaces have similar emissivities (Au: ~0.03, Al: ~0.04) and are spectrally flat in the 7-12μm range [*Horton, et al.*, 1998; *Salisbury and D'Aria*, 1992; *Salisbury, et al.*, 1994; *Touloukian and DeWitt*, 1970]. The downwelling spectral radiance is

$$L_D(\lambda) = \frac{L_A(\lambda) - \varepsilon_A(\lambda) B(T_A, \lambda)}{1 - \varepsilon_A(\lambda)} \qquad (1)$$

L_D = downwelling radiance
$L_A(\lambda)$ = measured spectral radiance from the aluminum foil (includes contributions from downwelling and the aluminum
$\varepsilon_A(\lambda)$ = emissivity of aluminum foil
$B(T_A,\lambda)$ = Planck blackbody spectral radiance of the aluminium foil
T_A = temperature of the aluminium foil

The Absolute emissivity of the rock surface is retrieved using

$$\varepsilon_S(\lambda) = \frac{L_m(\lambda) - L_D(\lambda)}{B(T_S, \lambda) - L_D(\lambda)} \qquad (2)$$

T_S = temperature of the rock surface
ε_S = absolute emissivity of rock surface

Three parameters are variable, ε_A, T_A and T_S. Of these, sample temperature has the greatest influence on the resultant atmospheric correction [*Horton, et al.*, 1998]. The effect of errors in the measured temperature of the aluminum foil is minimal due to its low emissivity. The temperature of the foil was difficult to measure anyway, so we used a temperature of 21°C (near ambient). *Horton et al.* [1998] found that halving or doubling the emissivity value of a gold plate resulted in a maximum error of only 2% in surface emissivity. Any minor variances from the 0.04 emissivity used for aluminum foil in the 7-12μm range should therefore produce less than 2% error in surface emissivity.

The sample temperature was measured using an Omegascope (a TIR temperature gun). An accurate reading depends on knowing the emissivity of the target, which is what we are trying to find out: we assumed an emissivity of 1. Therefore the temperature measurement is only approximate. Using the measured temperature as a starting point, T_s is adjusted in equation 2 until the atmospheric features are minimized (Figure 21).

APPENDIX B
DESCRIPTION OF AHI SYSTEM

AHI was designed and constructed by the University of Hawaii's Hawaii Institute of Geophysics and Planetology (HIGP) [*Lucey, et al.*, 2004; *Lucey, et al.*, 1998]. The AHI system consists of a TIR push broom hyperspectral imager and a boresighted 3-color visible high resolution CCD linescan camera. The TIR sensor consists of four subsystems: Telescope, spectrograph, background suppressor and FPA and associated electronics. The telescope is a 2-element diffraction limited transmission lens with 111 mm focal length and a 35 mm clear aperture. The spectrograph is an uncooled commercial reflective f/4 imaging spectrograph with gold-coated optics. It is possible to use an uncooled spectrograph and still achieve high performance because of the AHI background suppressor. The AHI uses a 256 x 256 element Rockwell TCM2250 HgCdTe focal plane array (FPA) mechanically cooled to 56K. In addition to having high quantum efficiency and pixel yields, it has excellent residual nonuniformity after correction (0.08%).

The AHI TIR system is radiometrically calibrated using a temperature adjustable flat plate blackbody that is observed thru the entire optical train. Two temperatures are used to produce pixel-dependent gain and offset corrections from DN to radiance. The temperatures are set to bracket the range of scene temperatures. A third temperature intermediate between the calibration temperatures is used to calculate the signal to noise ratio. Data for the intermediate temperature blackbody is collected and reduced to radiance as if it were target data, and the signal to noise is calculated over all the calibrated pixels for each wavelength so that spatial nonuniformity noise is included in the calculations. For many sensors spatial nonuniformity artifacts are the major source of noise so it is important to include this term in SNR measurements. Calibrations are performed frequently as calibration degrades relatively rapidly with time, with signal to noise dropping by a factor of two over the period of an hour and 10% in the first 5 minutes owing to increased residual nonuniformity noise. Wavelength calibration is accomplished by viewing our highest temperature blackbody through polystyrene plastic film. The polystyrene film is convenient to use in the field and has sufficient spectral absorptions to discern any problems with wavelength calibrations.

APPENDIX C
AHI DATA COLLECTION AND PROCESSING

Principal Component Analysis

In TIR spectrometry, the bands tend to be highly correlated. The spatial variations in spectral properties are subtle, and tend to be overridden by strong temperature variations [personal communication with Paul Lucey]. Principal Component Analysis (PCA) is a mathematical procedure used to view variation within a data set that has more data points than variables. The outputs are uncorrelated PC bands; each contains information on some variation within the data set. For TIR, the first PC band (PC1) tends to be highly correlated to temperature. The second PC band (PC2) usually is correlated to the major spectral band (i.e. the B feature in my study), and in practice may also be associated with the amount of vegetation (if present). The remaining PC bands may highlight subtle variations in band shape, such as relative depths of the three bands identified in the lab spectra. To create the flow maps, I used the first three PC bands, assigning PC1 to red, PC2 to green, and PC3 to blue. The resulting images have been georectified, resulting in non-strait images.

Emissivity

To derive emissivity information from TIR radiance spectra, atmospheric contributions need to be removed from the data. Atmospheric correction was done following the procedure discussed by *Young et al.* [2002] for in-scene atmospheric compensation (using information within the image scene to determine atmospheric contributions). A brief summary of the procedure is given here for the sake of discussion, for more details see *Young et al.* [2002]. The surface radiance, L_s, is recoverable from the observed radiance, L, using the compensation formula

$$L_S(\lambda) = \frac{L(\lambda) - L_U(\lambda)}{\tau(\lambda)} \qquad (3)$$

where $L_u(\lambda)$ is the upwelling atmospheric radiance and $\tau(\lambda)$ is the atmospheric transmittance. For naturally occurring blackbody surfaces, the equation

$$L(\lambda) \cong B(\lambda,T)\pi(\lambda) + L_U(\lambda) \qquad (4)$$

is used to approximate $\tau(\lambda)$ and $L_u(\lambda)$, where $B(\lambda,T)$ is the blackbody radiance. Vegetation such as tree groves, are generally a good approximation to a blackbody. There are two tree groves in the study area that were imaged by runs 1, 3 and 5.

Ideally, a wavelength is chosen where the atmosphere does not modify the target's surface radiance, and the target emissivity is assumed to be 1 (i.e. a blackbody). The wavelength of 11.1μm was chosen, because MODTRAN atmospheric profiles indicate an atmospheric window at this location; and, the spectral features identified in laboratory spectra (A, B and C) are not centered near this location. MODTRAN is a program that models atmospheric path radiance and transmission. It is maintained by the US Air Force Research Laboratory, Space Vehicles Directorate at Hanscom AFB in Bedford, MA. Figure 22 shows the modeled transmission spectrum for the default tropical model in a rural area.

A scatter plot (Figure 23) is made of $L(\lambda)$, versus $B(\lambda,T_b)$ for each spatial point in the image. A line is fit through the top of the scatter plot using Kolmogorov-Smirnov statistics to pick non-outlier points across the top of the scatter plot. The slope and intercept of the resultant lines gives $\tau(\lambda)$ and $L_u(\lambda)$, respectively. Plugging these into equation 3 gives the surface radiance. For scenes with adequate blackbody coverage, no prior knowledge of blackbody location is need; the routine will isolate pixels containing blackbody spectra. However, due to the paucity of vegetation in the study area, areas of vegetation were isolated to retrieve the atmospheric compensation parameters, which were then applied to the whole scene. If the whole scene was used to extract atmosphere compensation parameters, then the silicate bearing surface material dominates the algorithm and rock features may be removed inappropriately. Also, only runs 1, 3 and 5 had tree groves in them. Initially I used the TIR spectra of vegetation from run 5 for atmospheric compensation of all the runs. All the runs were completed during one hour, and there was no significant elevation difference between runs, so the atmospheric contributions should be similar.

However, after extracting emissivity (see below) only run 5 spectra seem to be mostly free of atmospheric contributions. A broad feature from 9-11μm, probably due to ozone, was apparent in all the spectra except those from run 5. We used vegetation from run 3 to correct run 3 for atmospheric contributions, and the broad feature was removed (Figure 24). Apparently atmospheric contributions and possibly instrument fluctuations are significant enough between runs to require run specific atmospheric corrections.

The atmospheric correction routine introduced a sharp spike at 11.1μm (Figure 25). This is probably due to the assumption that there is no atmospheric contribution at this wavelength. Because of this assumption, the value at this wavelength is not adjusted; however, all other bands are adjusted downward resulting in a sharp spike. This spike is carried into the derived emissivity spectra. The resultant spectra also seemed to have noise introduced. Possibly due to the assumption that the trees behave like a blackbody in the 7-12μm region.

Because of these issues, I modified the routine to use known emissivity values (collected in the lab and in the field) of the 4-8ka pahoehoe unit in place of the assumed blackbody (tree groves). This eliminates the need to assume the trees have an emissivity of 1. So for equation 3, we substitute $L_k(\lambda,T)\varepsilon_k(\lambda)$ for $B(\lambda,T)$, where L_k is the averaged AHI spectrum for the 4-8ka unit, and ε_k is the laboratory emissivity of samples taken from the same unit. After this modification, the resultant spectra had less noise, and visually look more like the lab and field spectra (Figure 25).

We used an assumed emissivity routine on the atmospherically corrected data to separate emissivity and ground temperature. The emissivity of a real material is defined as

$$\varepsilon(\lambda) = \frac{L_S(\lambda, T)}{B(\lambda, T)} \qquad (5)$$

Where L_s is the radiance of a real material (in our case the atmospherically corrected surface radiance) and B is the blackbody radiance. We can derive the emissivity by first finding the temperature of the target at a wavelength (11.1μm) where we can make a reasonable assumption that the emissivity is approximately equal to 1, using:

$$T(\lambda, B) = \frac{c_2}{\lambda \ln\left(\frac{c_1}{\lambda^5 L\varepsilon} + 1\right)} \qquad (6)$$

Were $c_1 = 1.19104 \times 10^{10}$ μm⁴-μW/cm²/sr and $c_2 = 14387.7$ μm-K are radiation constants, T is the temperature, L is the radiance, ε is the assumed emissivity (equal to 1) and λ is the wavelength. This temperature is then used to calculate the blackbody radiance at each wavelength using

$$B(\lambda,T) = \frac{c_1}{\lambda^5 (e^{c_2/\lambda T} - 1)} \qquad (7)$$

This blackbody radiance and the atmospherically corrected surface radiance (L_s) are then plugged into equation 5 to get the emissivity. The derived ground temperature mean was 295 ± 5 K. The resultant emissivity spectra tended to have some values grater than 1 (maximum derived emissivity: 1.1), due most likely to the imperfect nature of assuming an emissivity for the reference band. Also the atmospheric correction routine is not perfect and residual atmospheric contributions could drive the apparent emissivity above unity. The spectra were normalized by dividing by the highest emissivity value.

TABLES

Table 1. Site names and sample descriptions. The prehistoric group ages (OP1,4,5,6,8,10) are grouped following Kahle et al. 1988 and are based on radiocarbon dates of recovered charcoal.

Site	Age	Precipitation	Site Descriptions
PO	0 (Kilauea)		Fresh pahoehoe has a glassy rind that is highly specular with a bluish purplish metallic luster. The shiny smooth surface spalls easily and reveals a shiny vesicular interior with a similar luster.
OP2	0.07 ka (1935 AD)	122 cm/yr	The1935 pahoehoe samples are vesicular with a metallic luster similar to the inside of the fresh pahoehoe samples. One sample is approximately 50% covered in a brown coating and has a dull luster
OP3	0.16 ka (1843 AD)	144 cm /yr	The pahoehoe has a dark diffuse surface and is slightly more reddish than the 1935 pahoehoe. The 1843 aa is similar in color to the 1843 pahoehoe.
OP1	0.2-0.5 ka	127 cm/yr	The pahoehoe has a smooth dull vesicular surface similar to kneaded bread and is dark reddish gray colored. The aa is of similar color to the pahoehoe. Area contains scattering of low lying brush. Looks similar to the older OP8 site.
OP10	0.2-0.5 ka	89 cm/yr	Same age as OP1 but looks more like OP 3. Has dark diffuse slightly more reddish than OP2; surface similar to OP3, though a bit rougher.
OP8	0.5-1.5 ka	99 cm/yr	Light gray and brown and rough. Looks similar to the younger OP1.
OP5	1.5-4 ka	109 cm/yr	The pahoehoe surface is a read/brown with some black specks. The surface is rough and dirty looking. The aa is much lighter in color than the pahoehoe.
OP4	4-8 ka	114 cm/yr	Similar to OP5. Light red-tan color.
OP6	>8 ka	104 cm/yr	Pervasively weathered and highly vegetated with brush. Much of the surface is tan soil, or rock with a coating of tan soil/dust.
OP7			Tree grove
OP9			Tree grove

FIGURES

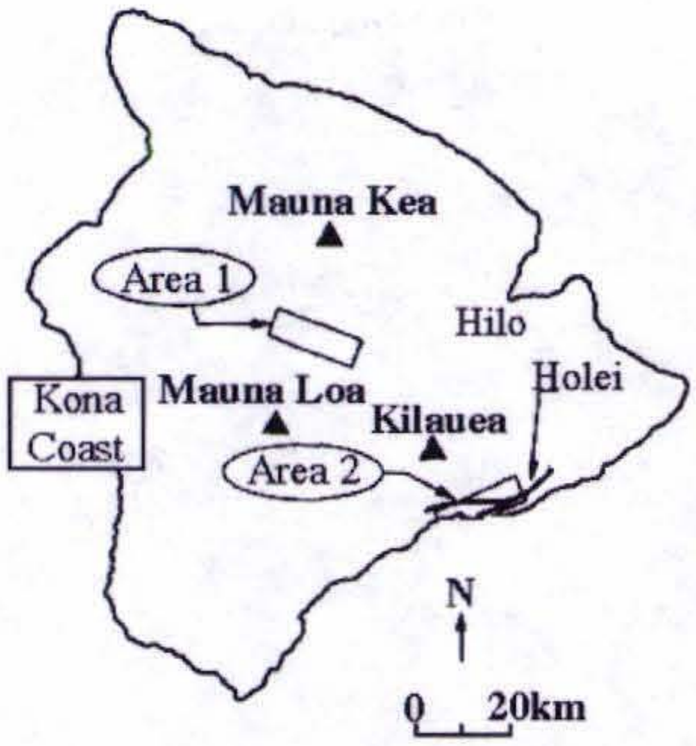

Figure 1 Map showing location of Kahle et al. study. (after Kahle et al. 1988). Detailed map of "Area 1" is shown in Figure 2.

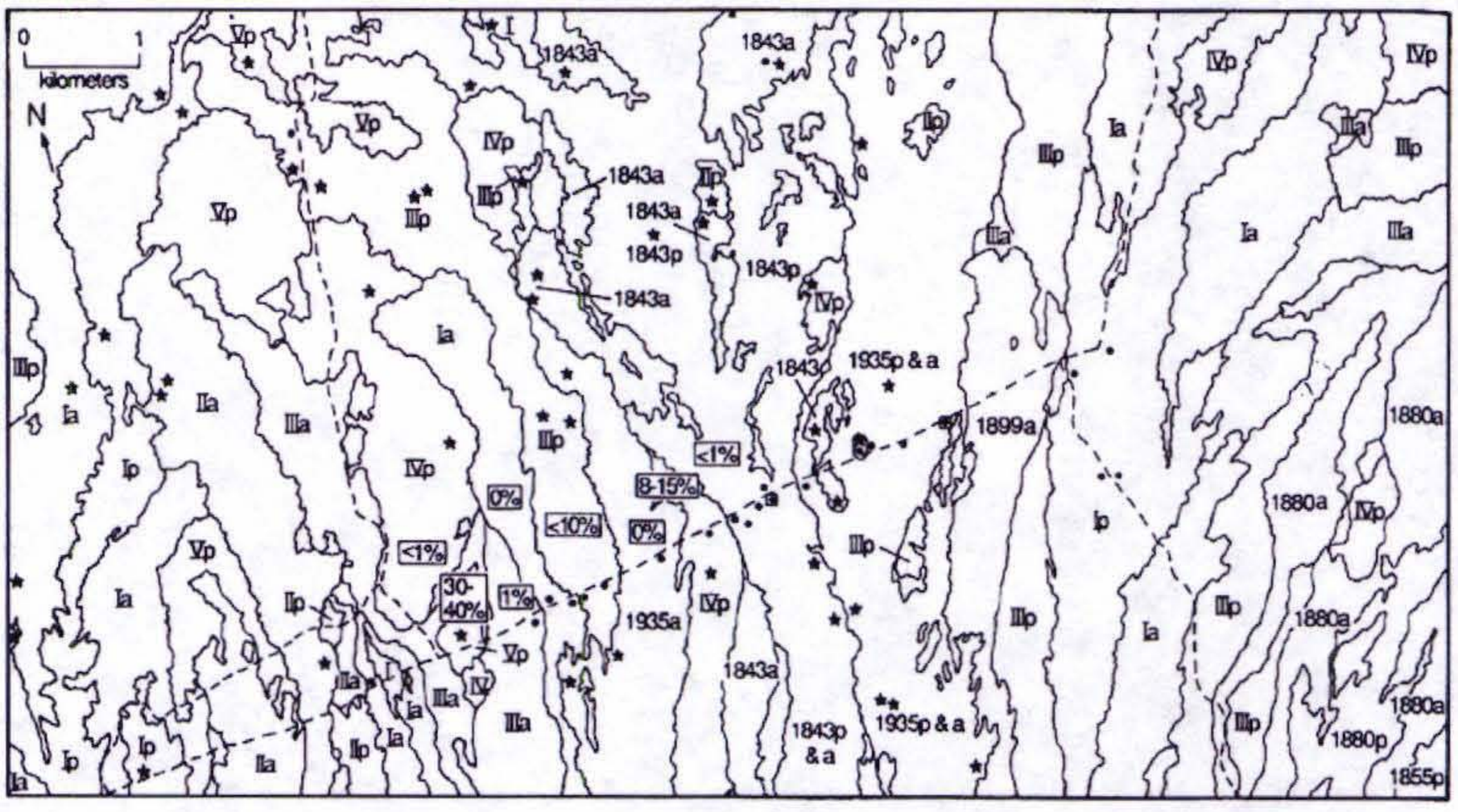

Figure 2. Detailed map of "Area 1" in Figure 1 (from *Kahle et al.* 1988). Circles mark location of samples used in figure 4. Stars indicate locations of TIMS data used to make figure 5. Map also shows flow ages; year of flow for historic flows; radiocarbon dates for historic which are groped as: I(0.2-0.5ka), II(0.5-1.5ka), III(1.5-4ka), IV(4-8ka) and V(>8ka). Flow types are given as: p for pahoehoe; a for aa; pa for pahoehoe-aa mix.

Figure 3. This is a PCT map of area-1 from the Kahle et al. study [1988]. TIMS channels 1, 3 and 5 were processed with a decorrelation stretch, and the resulting three bands were plotted as red, green and blue. See Figure 2 for index of flow ages. After *Kahle et al.* [1988].

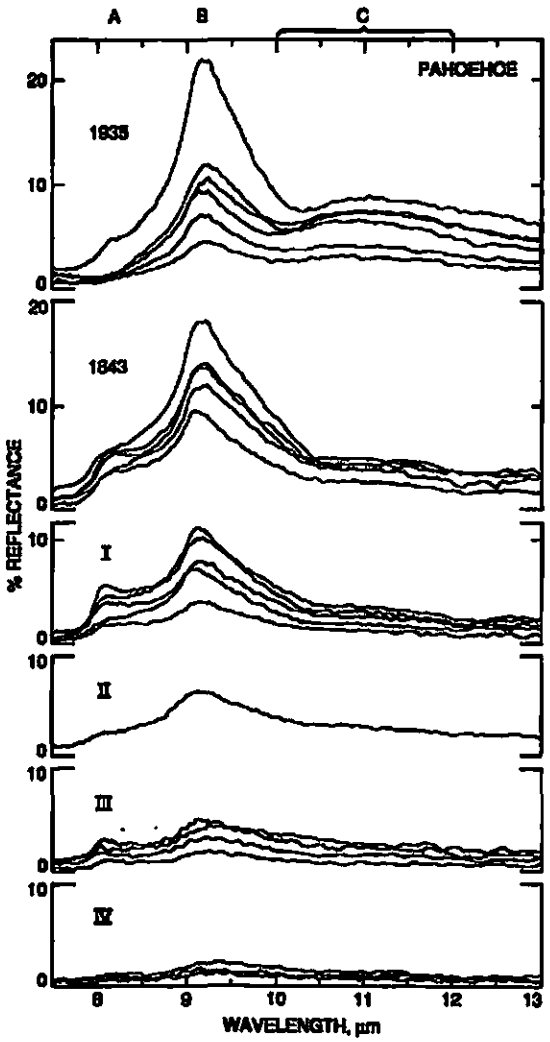

Figure 4. Laboratory spectra of pahoehoe from *Kahle et al.* 1988.

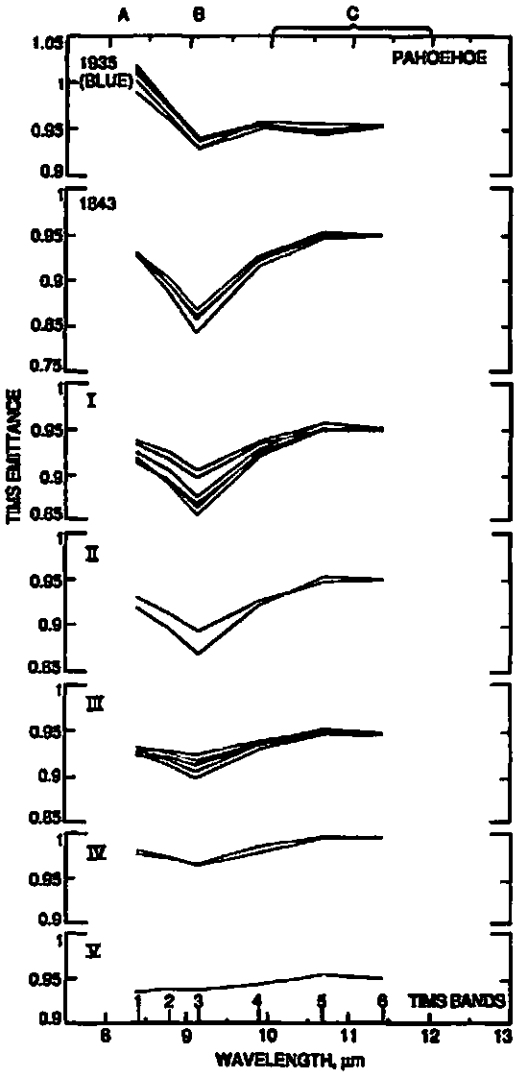

Figure 5. Spectra of pahoehoe taken with TIMS. Showing 9.2µm feature. Due to low resolution, the 8.2µm and 10.5µm features are not well defined, and show up as depressions of values at the ends of the spectra. From *Kahle et al.* 1988.

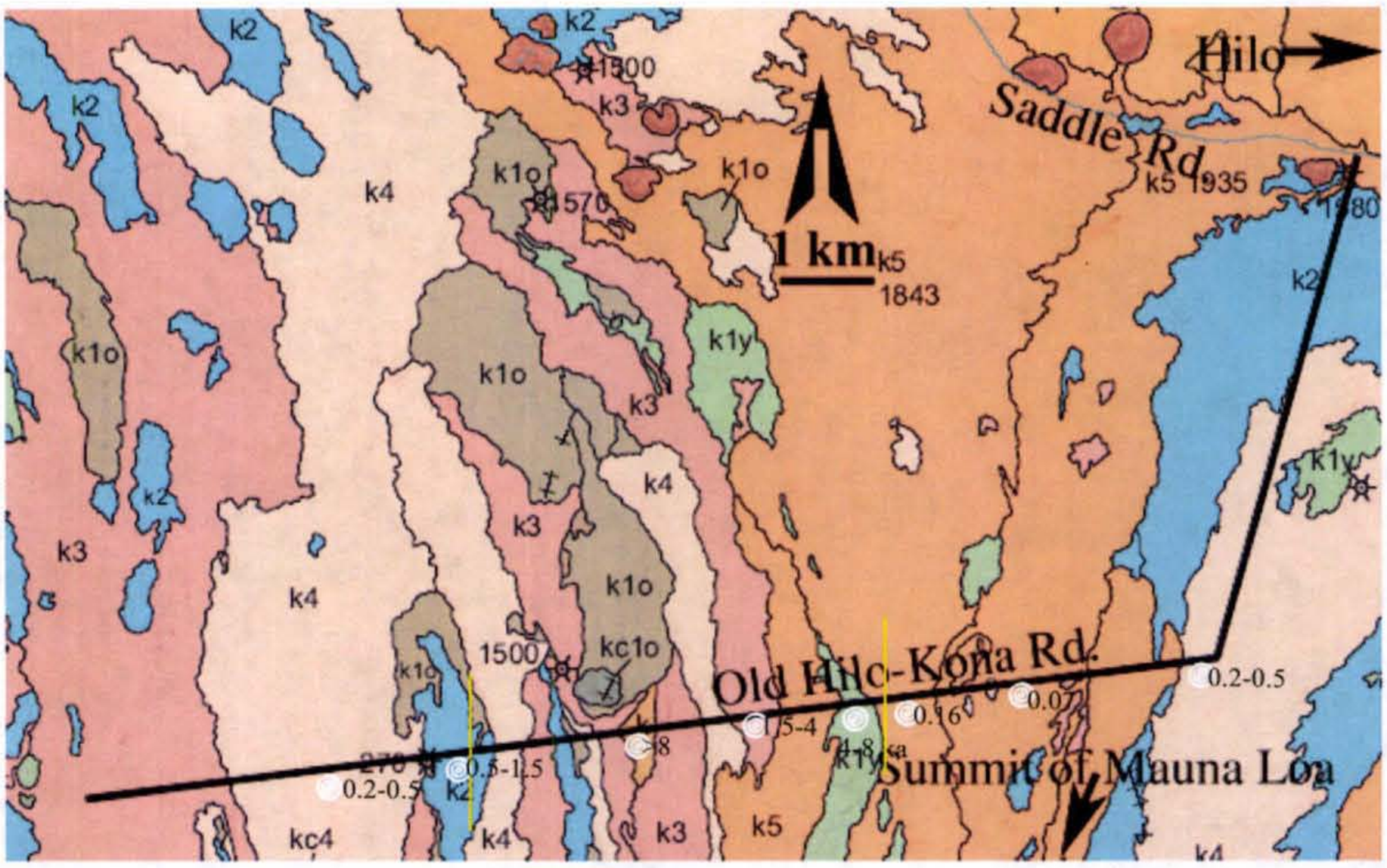

Historic, A.D. 1790 or younger

0.2-0.7 ka*

0.7-1.5 ka*

1.5-3 ka*

3-5 ka (younger)*

5-10 ka (older)*

>10 ka*

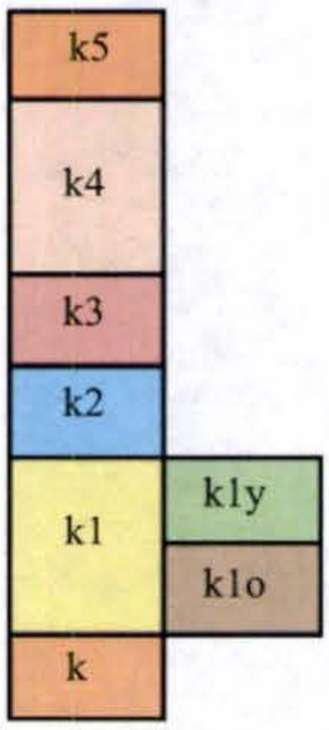

* Age in ^{14}C years

Figure 6. Map locating flight area. Background map is section of the USGS Geologic Map of the Island of Hawaii compiled by *Wolfe and Morris,* 1996. The ◎ symbol marks the sample and D&P location sites. The horizontal yellow lines show where Figure wraps.

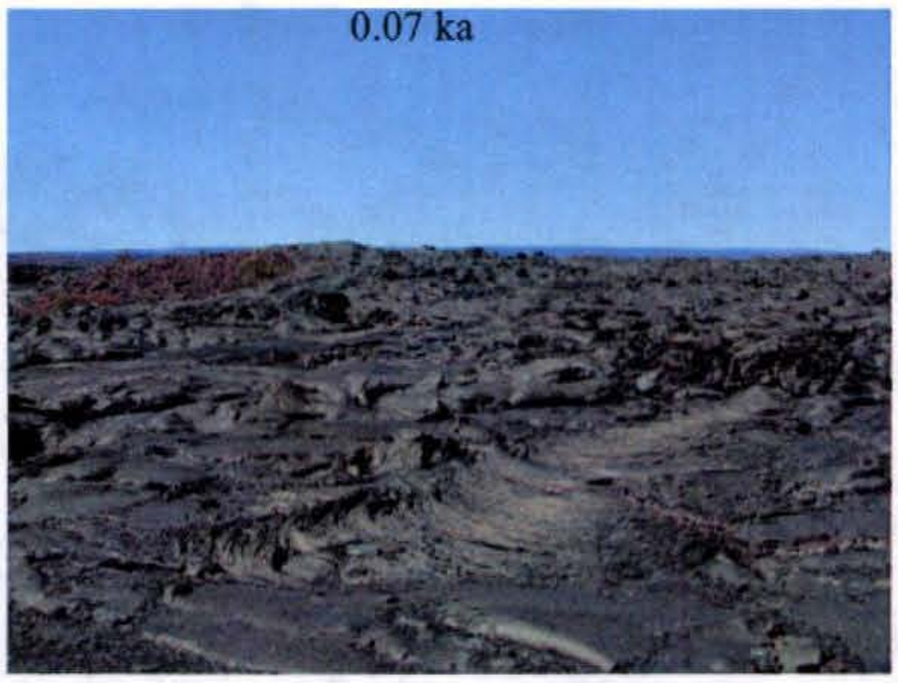

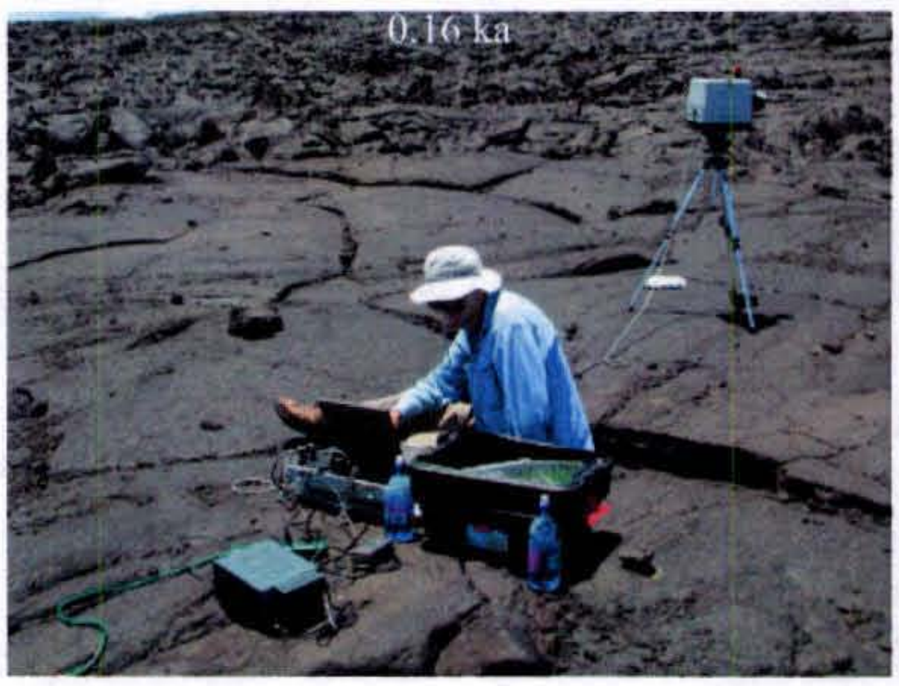

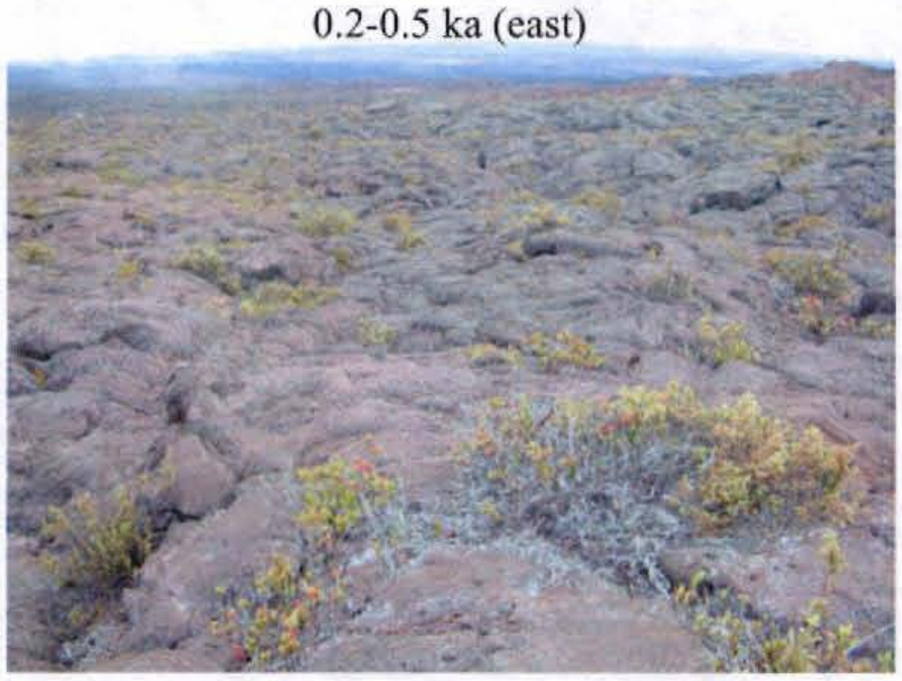

Figure 7. Younger flows (fresh - 0.5 ka). Notice the difference in weathering between 0.2-0.5 ka west and 0.2-0.5 ka east. The western branch of the 0.2-0.5 ka flow is black and is mostly void of vegetation, whereas the eastern branch is reddish gray and has obvious vegetation. The eastern branch of 0.2-0.5 ka looks more like the older flows in figure 8.

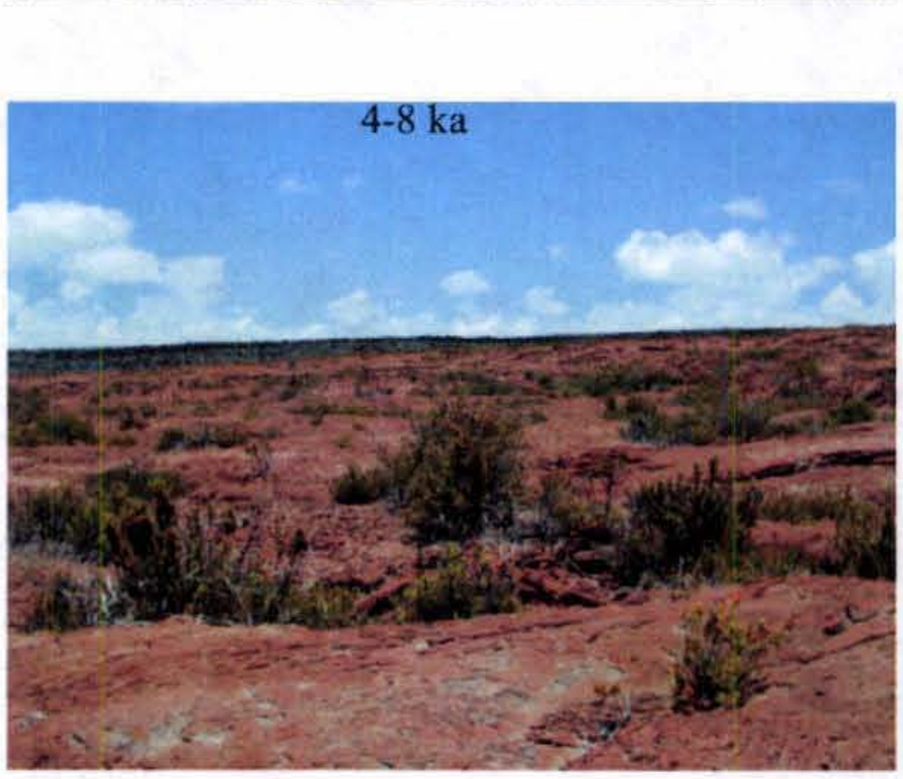

Figure 8. Older flows (0.5 - over 8 ka).

Figure 9. A mosaic false color image of all AHI runs. The data were processed with a principal components transform and then georeferenced. The flows are labeled with the unit date in thousands of years before present (ka). The date is followed by flow type: p = pahoehoe, a = aa, pa = mixed pahoehoe and aa. The aa varies only slightly between green and bluish-green, whereas the pahoehoe varies across a wide range of colors. The ◎ symbol marks the sample location sites. The figure has been wrapped to fit on page. Yellow lines in figure 6 indicate approximate points where figure wraps.

Figure 10. The D&P setup in the field.

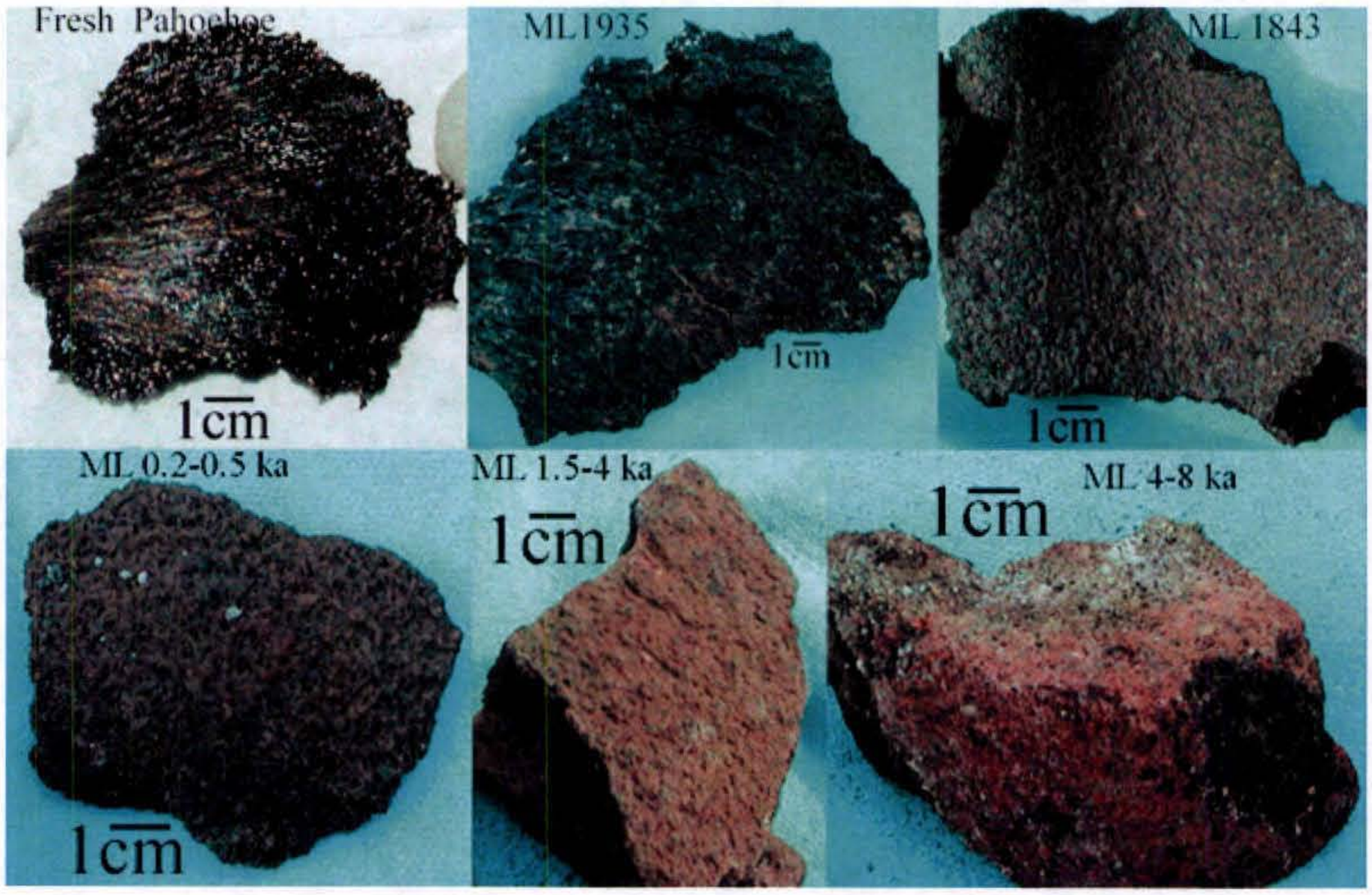

Figure 11. Samples collected from the study site.

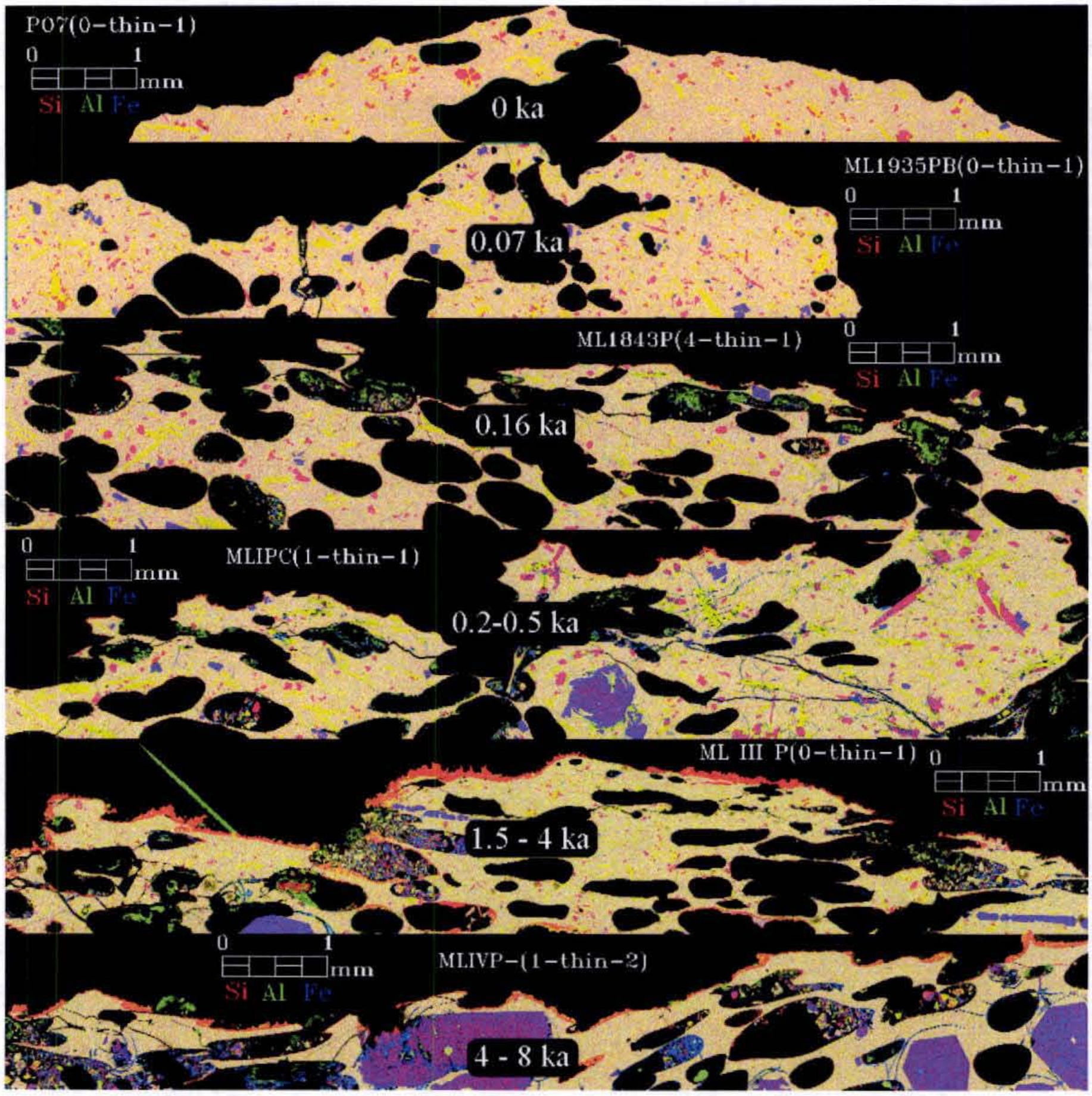

Figure 12. Microprobe image displayed as Si=red, Al=green, and red=blue. Silica-Aluminum rich coating shows up as orange on 0.17 ka and older flows. Younger samples show no sign of coating at 10 μm resolution.

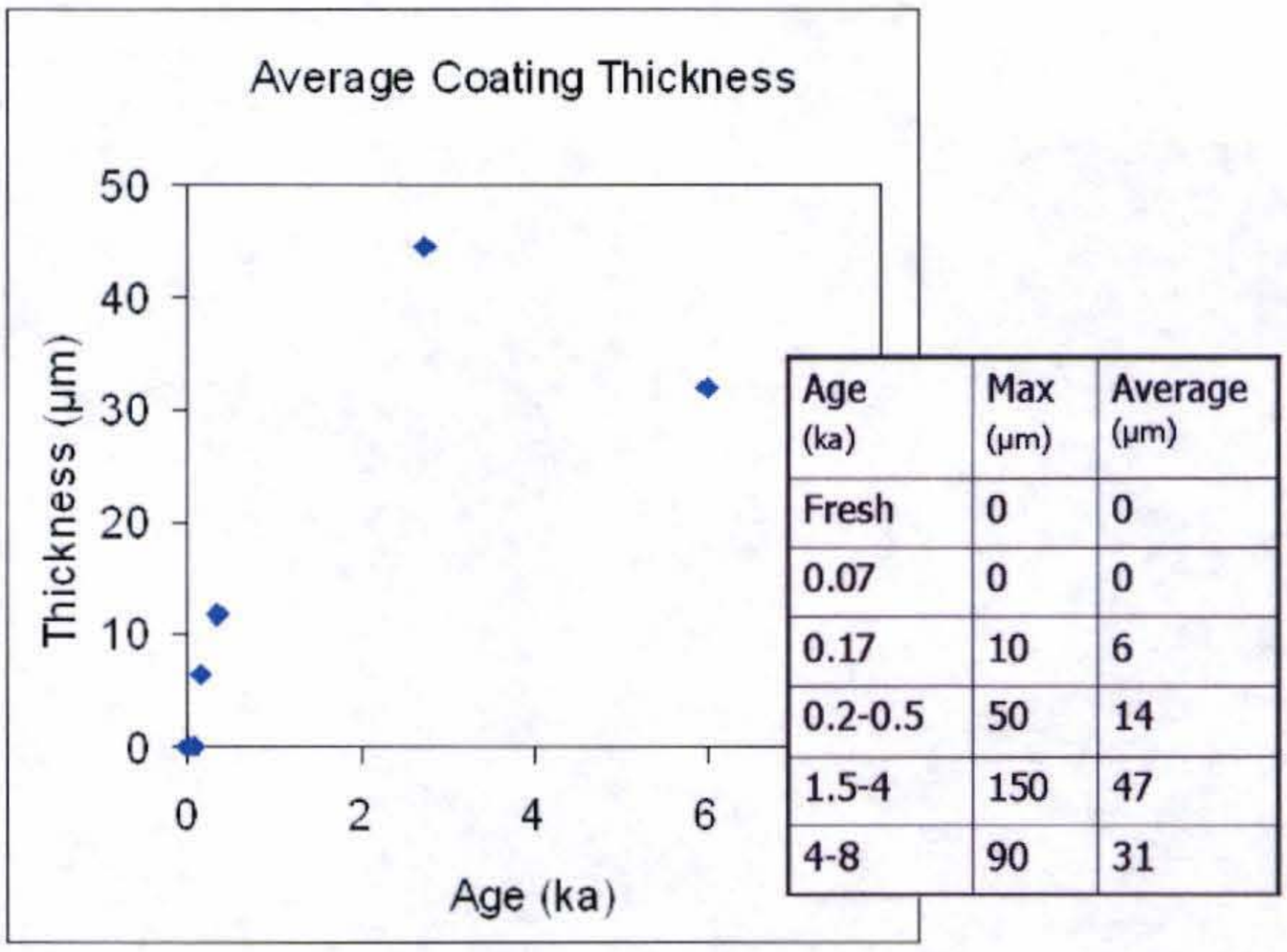

Age (ka)	Max (µm)	Average (µm)
Fresh	0	0
0.07	0	0
0.17	10	6
0.2-0.5	50	14
1.5-4	150	47
4-8	90	31

Figure 13. Coating thickness vs. age. Average thicknesse of silica coating as measured on microprobe images (Figure 12).

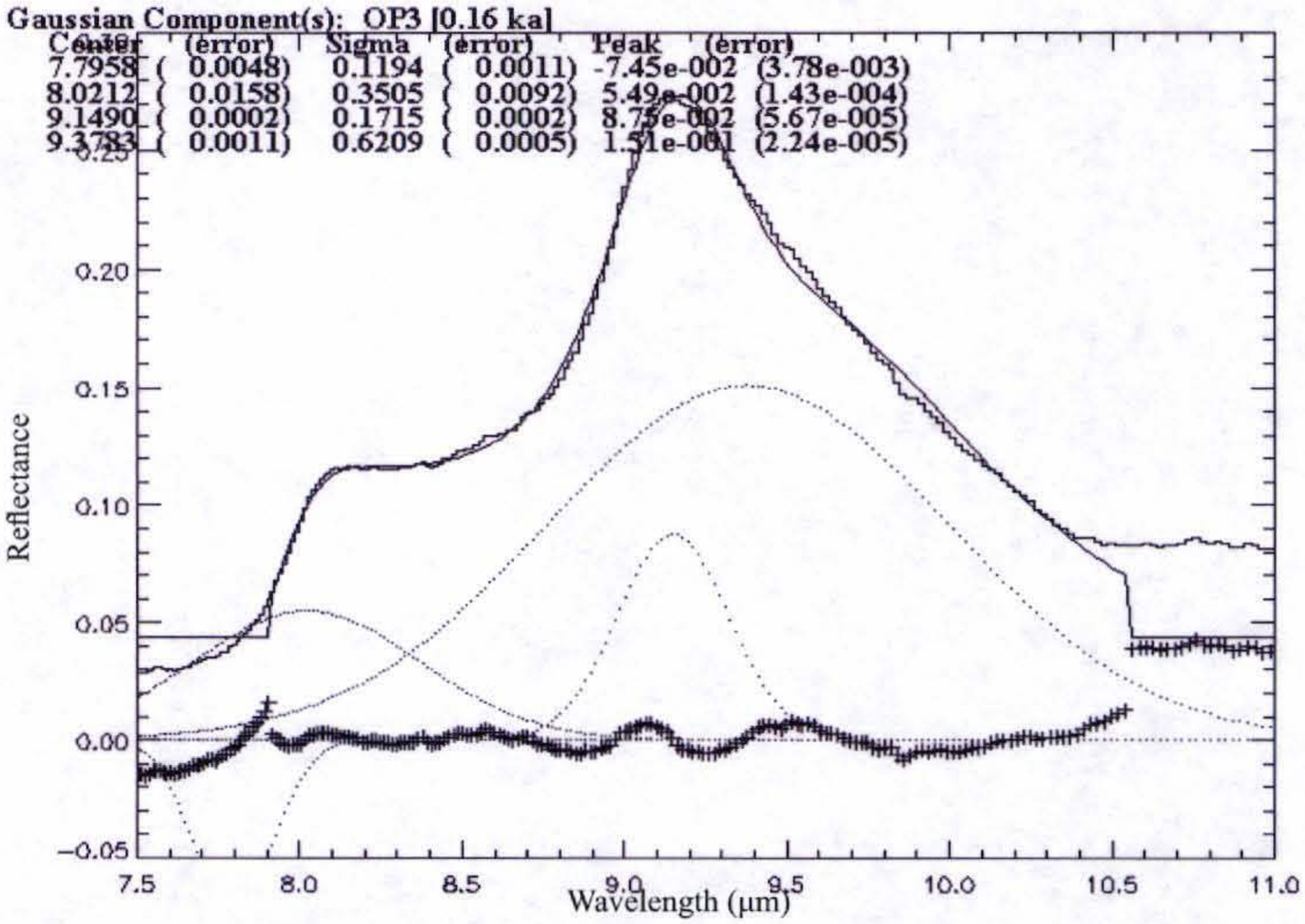

Figure 14. Plot of Gaussian fit over Nicolet reflectance data for a sample from the 0.16 ka flow. Each line of numbers at the top represent the center, sigma, peak hight and associated errors of one of the gaussian curves that make up the overall fit.

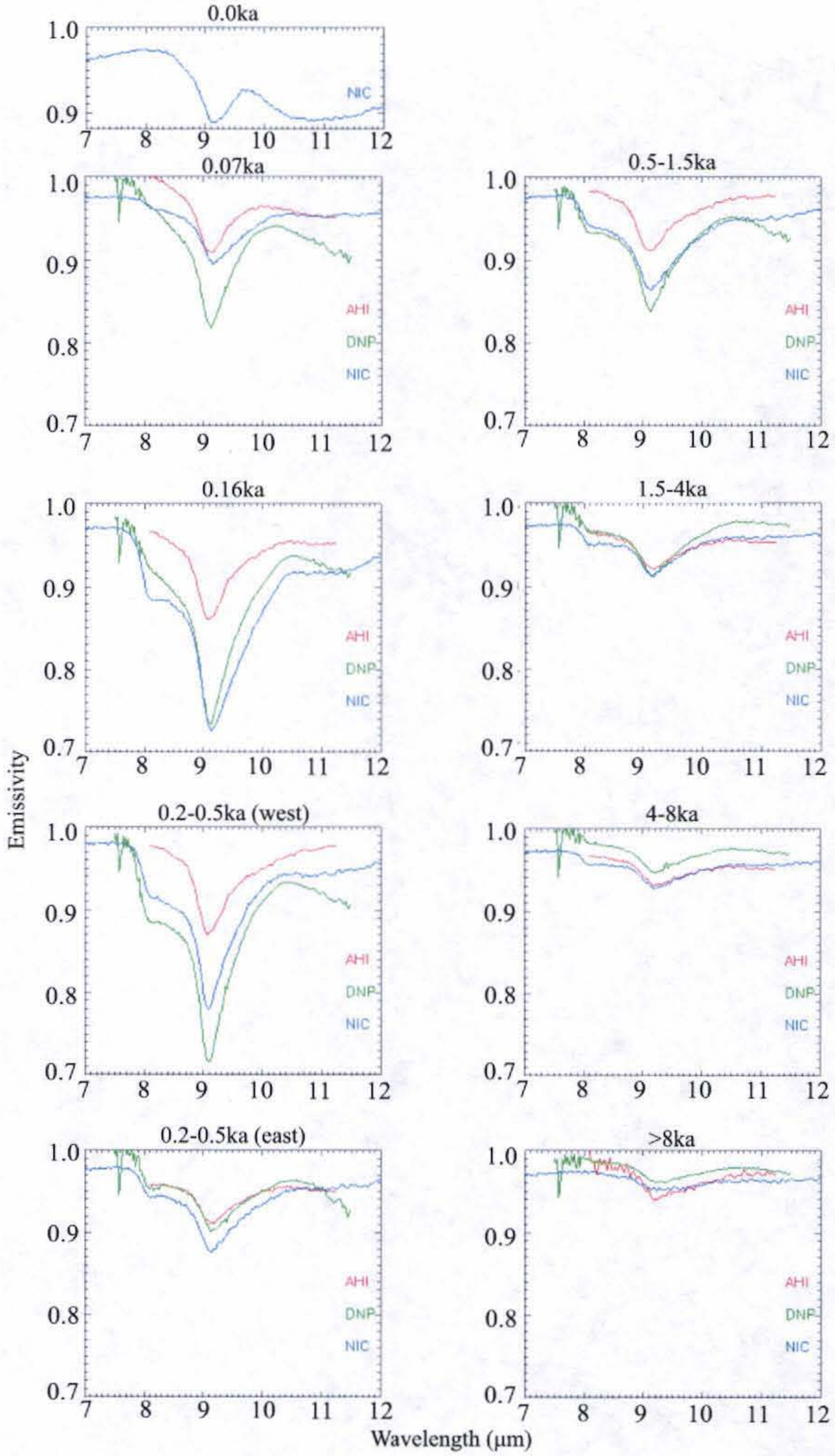

Figure 15. These plots compare the spectra collected from the AHI, D&P and Nicolet. Nicolet emissivity is derived from reflectance data using Kirchhoff's Law E=1-R.

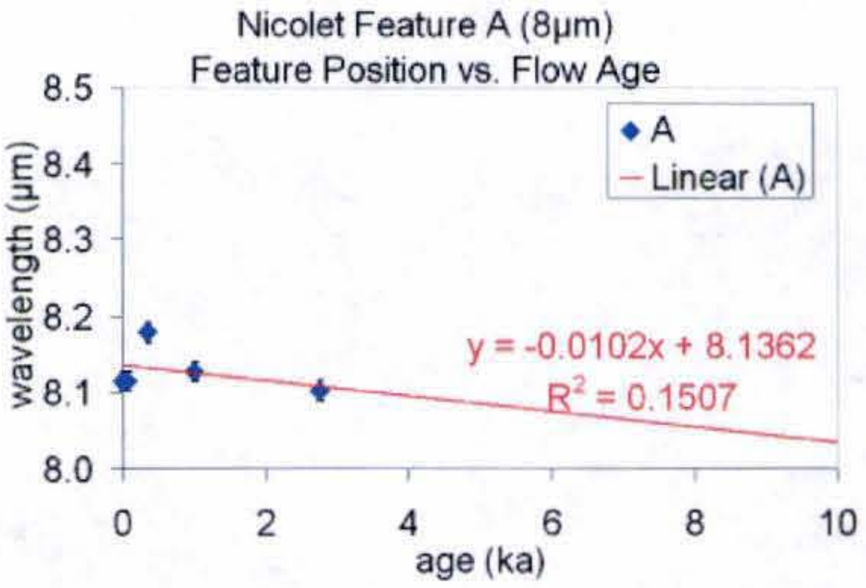

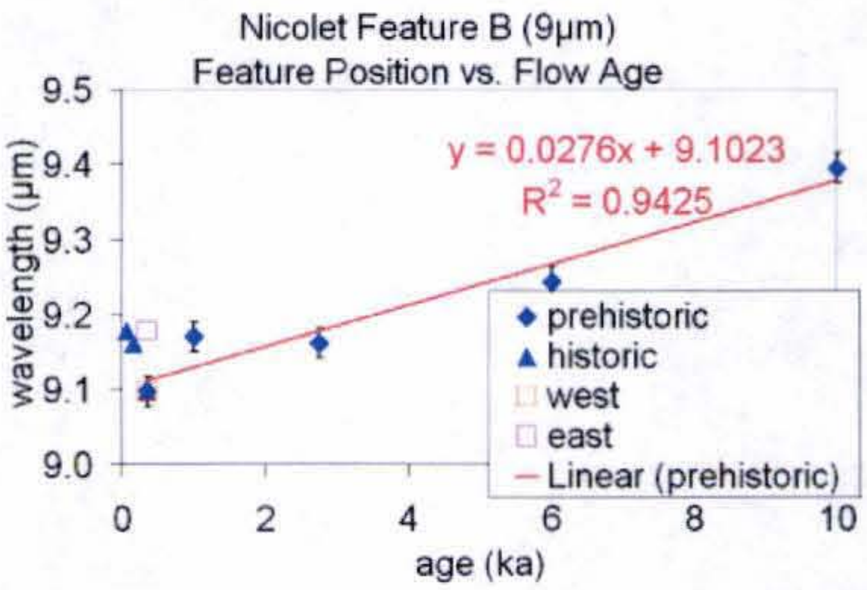

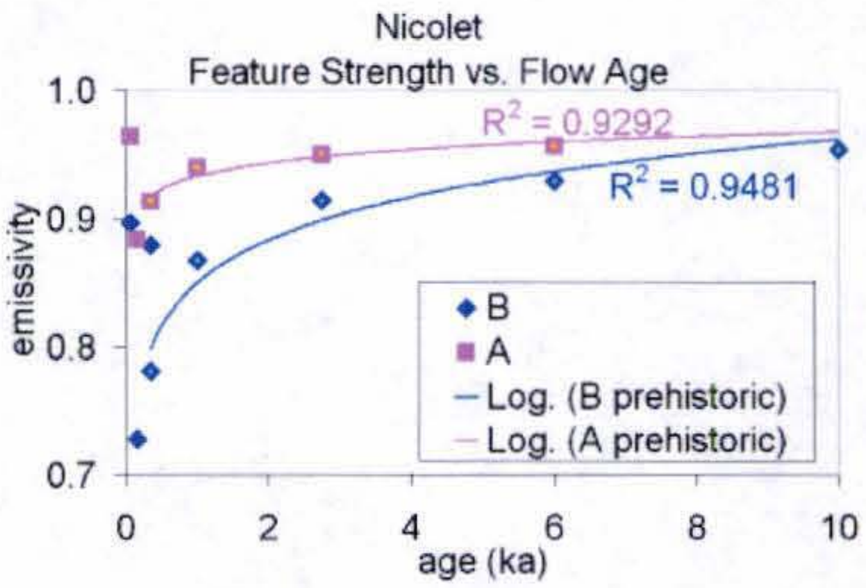

Figure 16. Age related trends in the laboratory (Nicolet) data. Top plot is the A feature position vs. age. The middle plot is the B feature position vs. age. The bottom plot is feature strength vs. age. All values are taken from Gaussian fits.

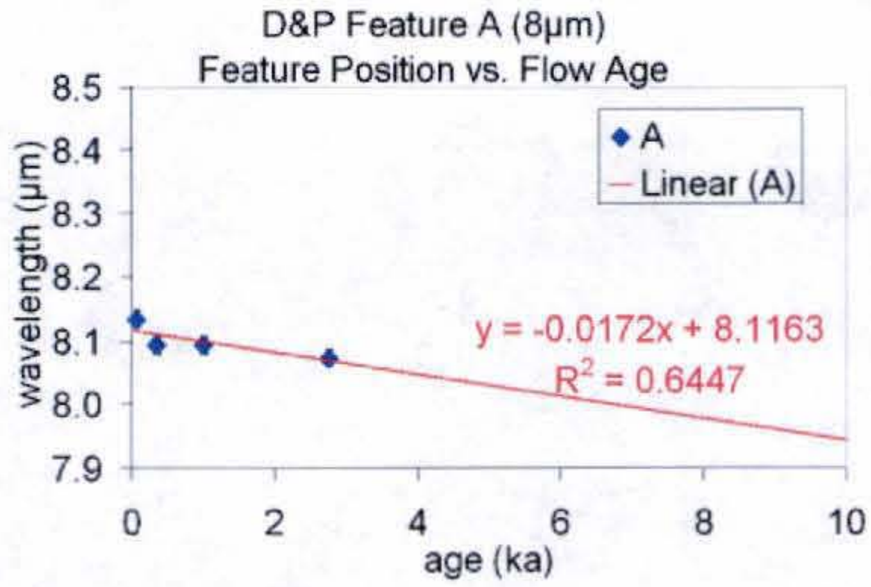

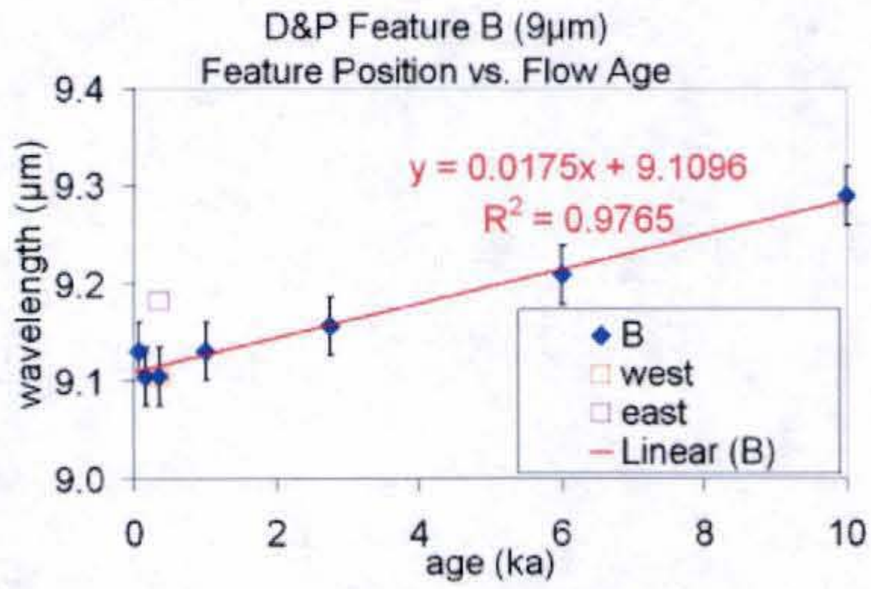

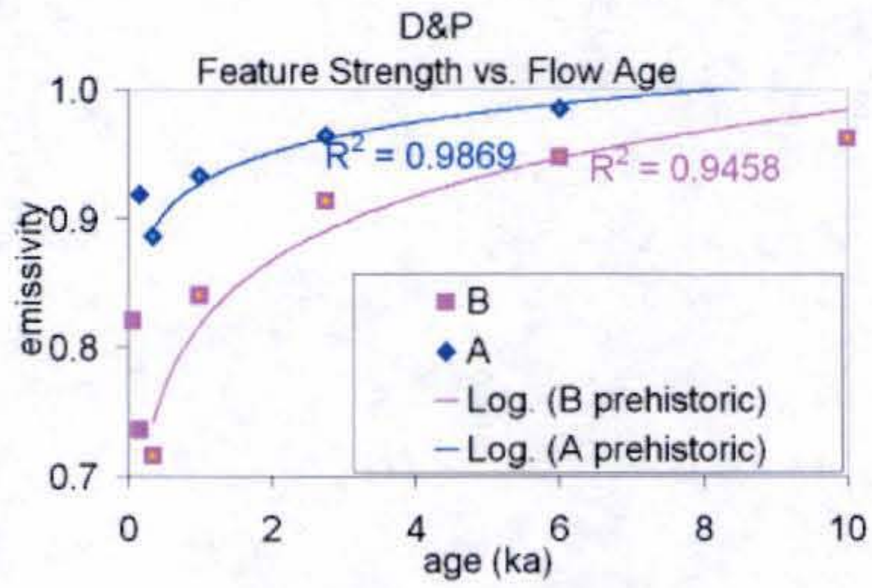

Figure 17. Age related trends in the field (D&P) data. Top plot is the A feature position vs. age. The middle plot is the B feature position vs. age. The bottom plot is feature strength vs. age. All values are taken from Gaussian fits.

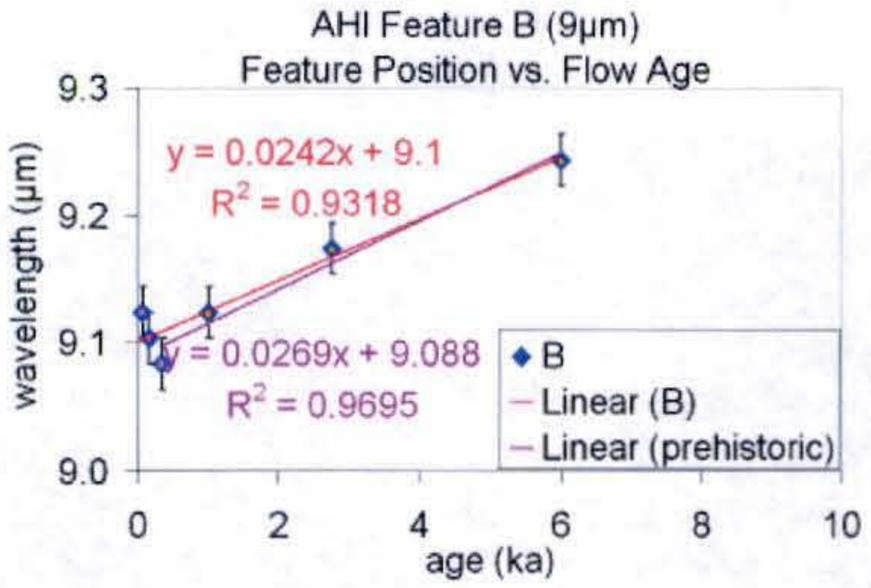

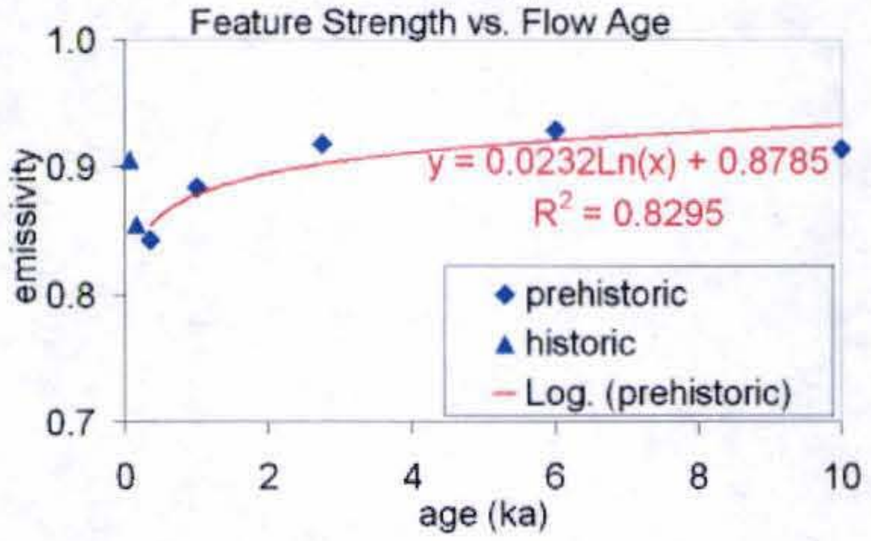

Figure 18. Age related trends in the AHI data. Top plot is the A feature position vs. age. The middle plot is the B feature position vs. age. The bottom plot is feature strength vs. age. All values are taken from Gaussian fits.

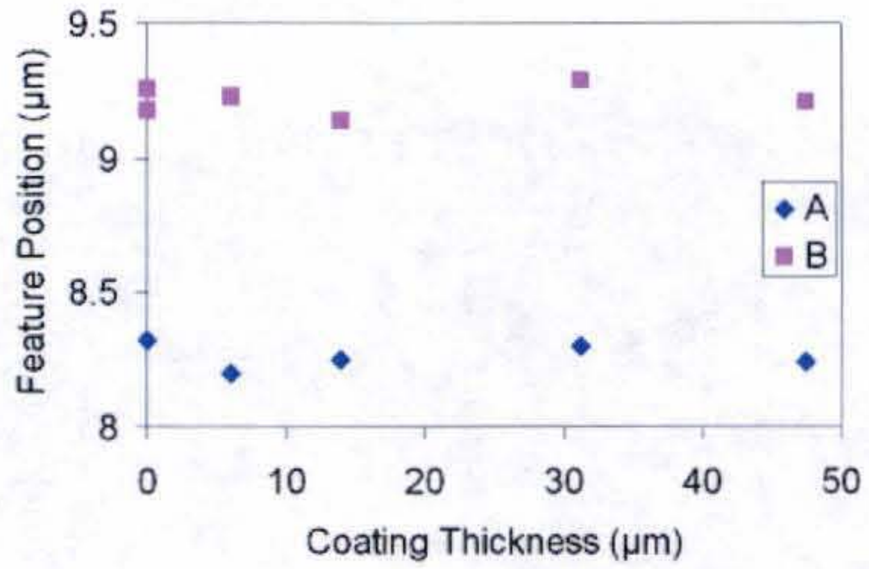

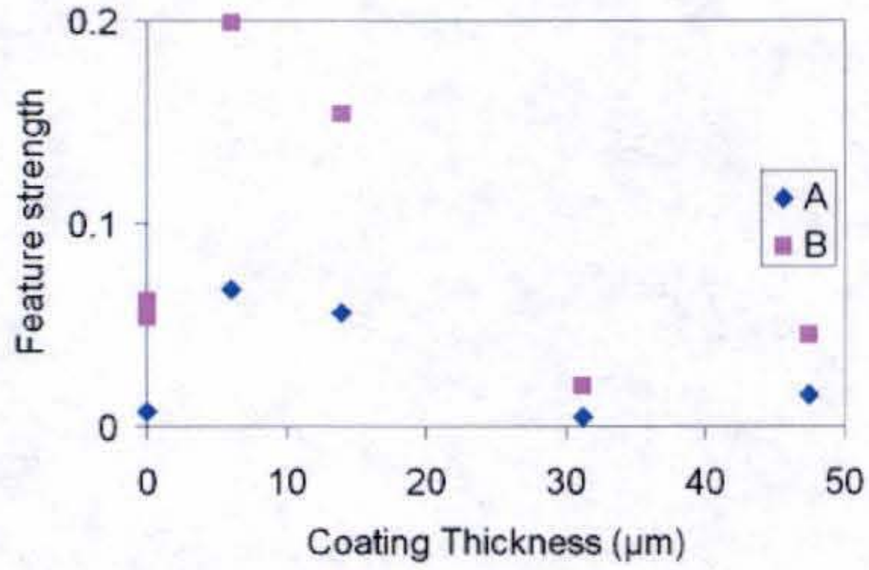

Figure 19. Feature trends vs. coating thickness. Coating thicknesses are averages taken from microprobe measurements. Feature position and strength are Gaussian parameters taken from Gaussian fits of laboratory spectra. Top plot is feature position vs. thickness. Bottom plot is feature strength vs. coating thickness.

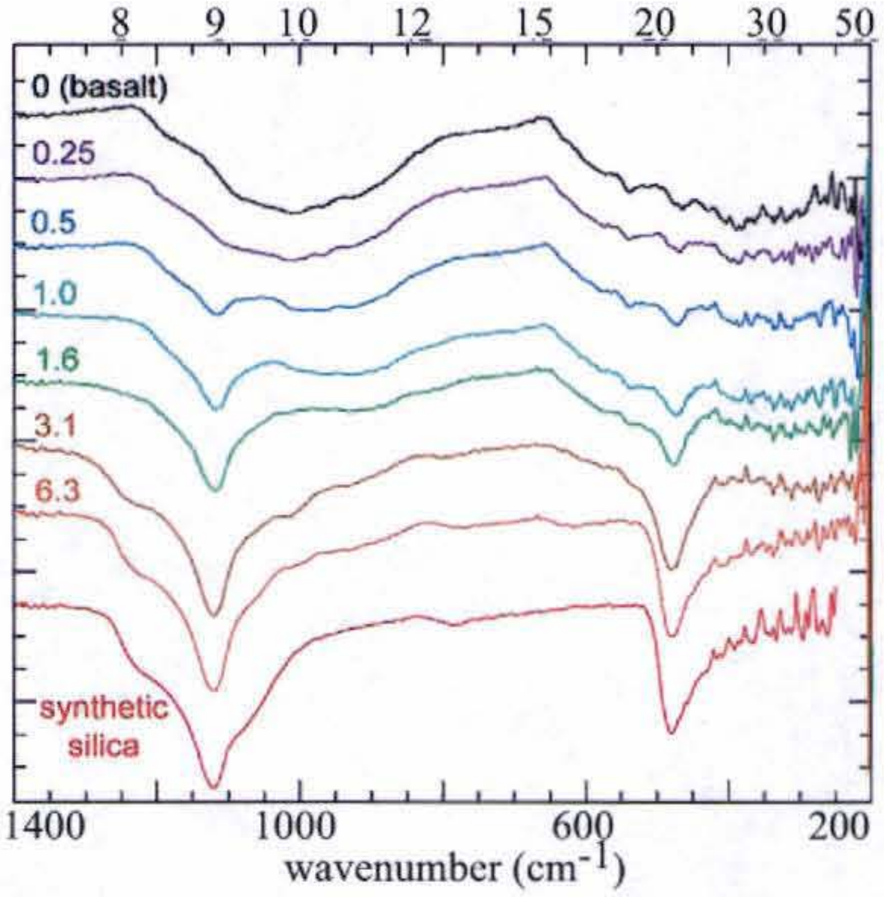

Figure 20. Thermal IR emission spectra of silica coated CRB. Coating thickness is given on the graph in micrometers. Y-axis is emissivity in increments of 0.05. Spectra are offset for clarity. From *Kraft et al.* 2003.

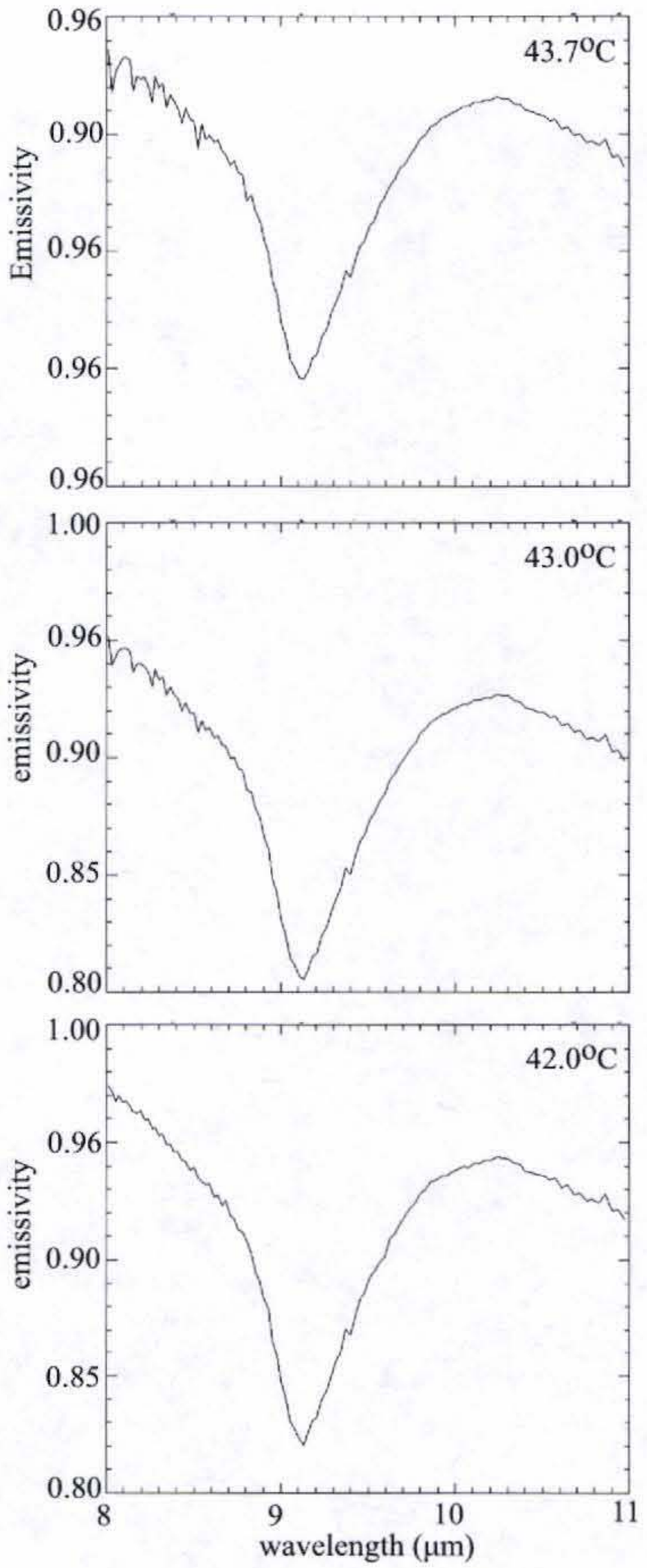

Figure 21. Example of D&P atmosphere correction. To correct for atmospheric effects the sample temperature is adjusted in the algorithm until the atmospheric contribution is minimized. In this example we start at the temperature measured in the field (43.7°C). The final temperature is 42.0°C, and results in a fairly clean emissivity spectrum.

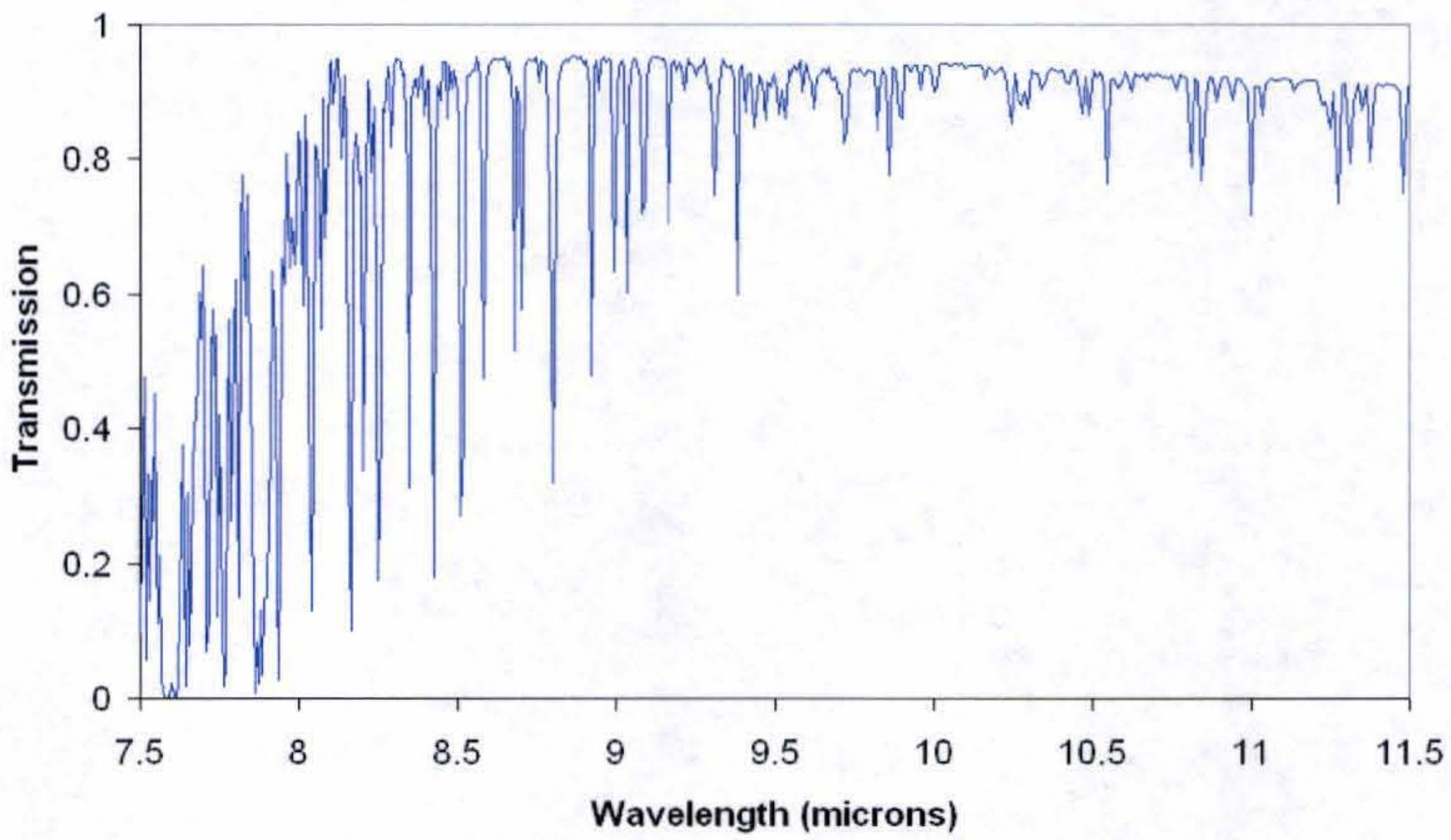

Figure 22. MODTRAN modeled atmospheric transmission profile for the default tropical model in a rural area. Instrument altitude is set at 3km and the ground elevation is set at 2km.

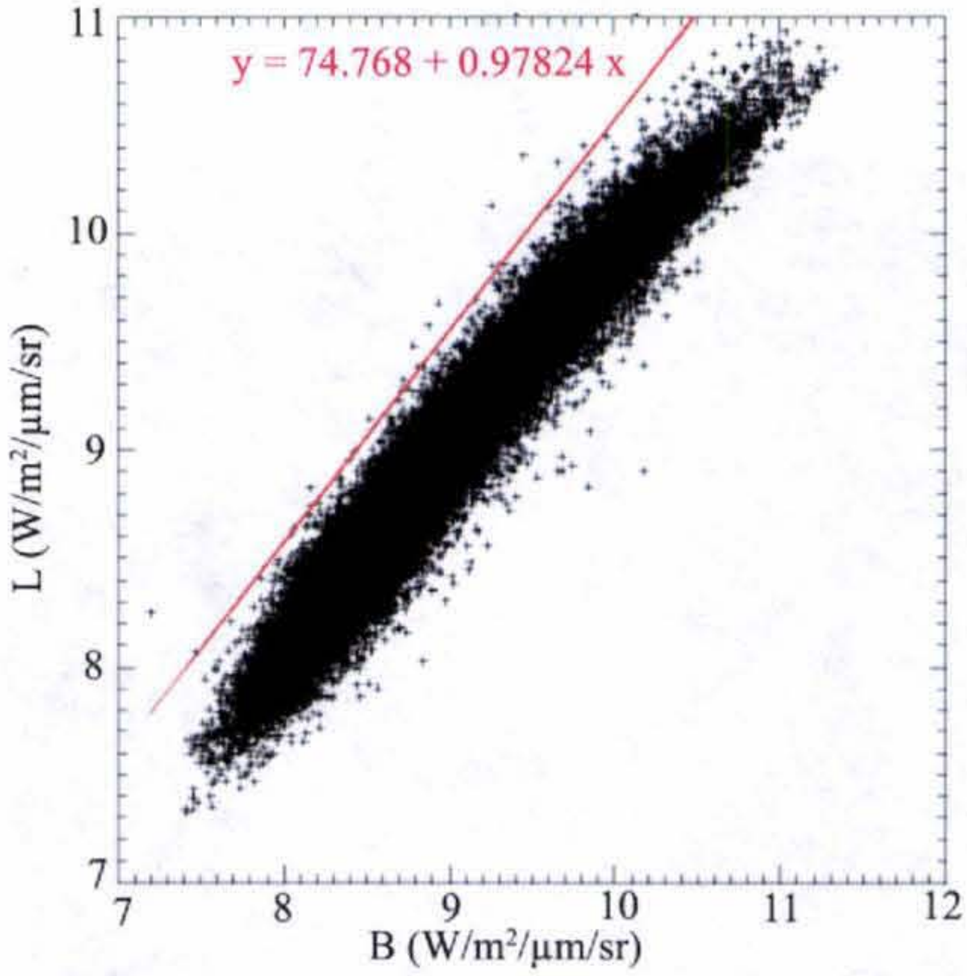

Figure 23. AHI atmospheric correction routine plots observed radiance at instrument (L) versus blackbody radiance (B). A line is fit through the top of the scatter plot using Kolmogorov-Smirnov statistics.

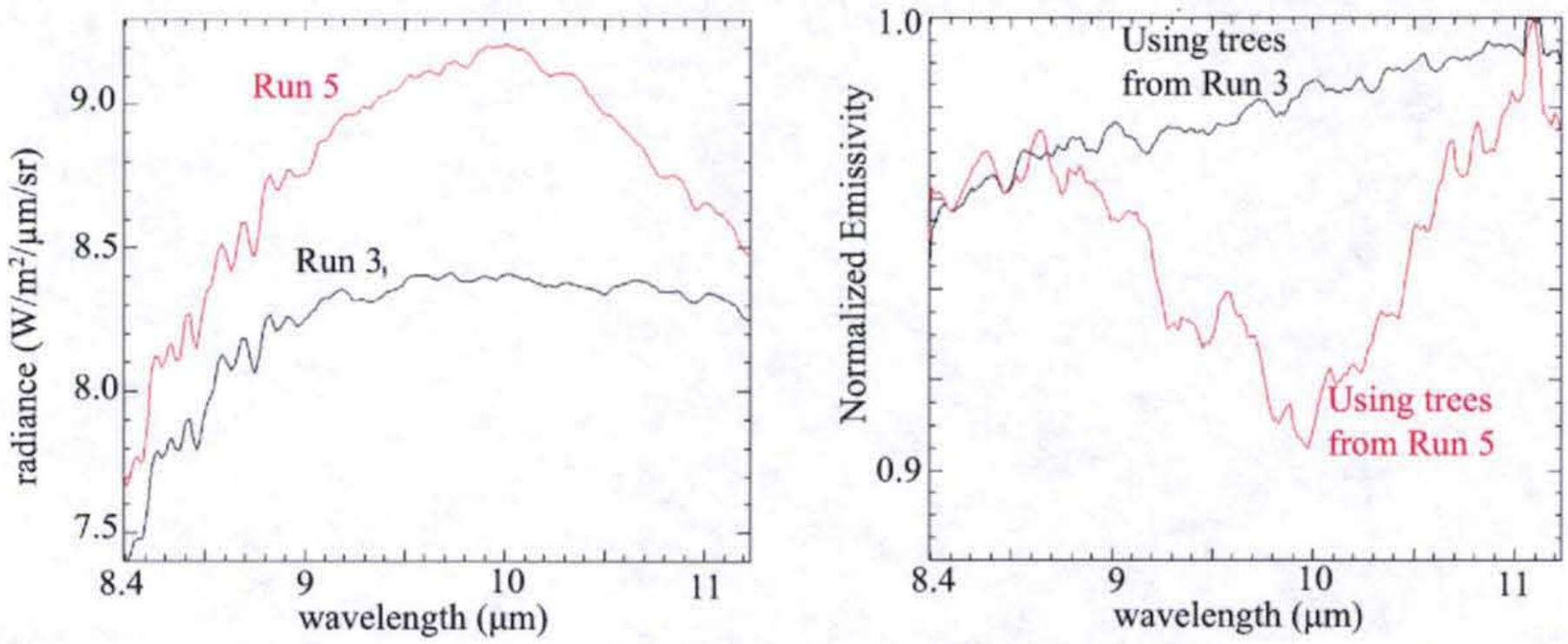

Figure 24. Comparing effect of using vegetation from one run to correct for atmospheric contribution in another run. The left plot is of radiances for trees from run 3 and run 5. Radiances are averaged over area of trees, and are not corrected for atmosphere. Notice significant difference in shape. Right plot is of emissivity spectra from trees from run 3 using trees from run 3 and trees from run 5. Using trees from run 5 on run 3 does not remove all the atmospheric contributions (the big dip around 10µm is probably ozone). Using run 3 on run results in flatter spectra as is expected. This means that atmospheric corrections for each run must use approximate blackbody sources with in that run to derive the atmospheric contribution. However there is a spike at 11.1µm and a slope to the left which may be a result of the assumption that the atmosphere is transparent at 11.1µm

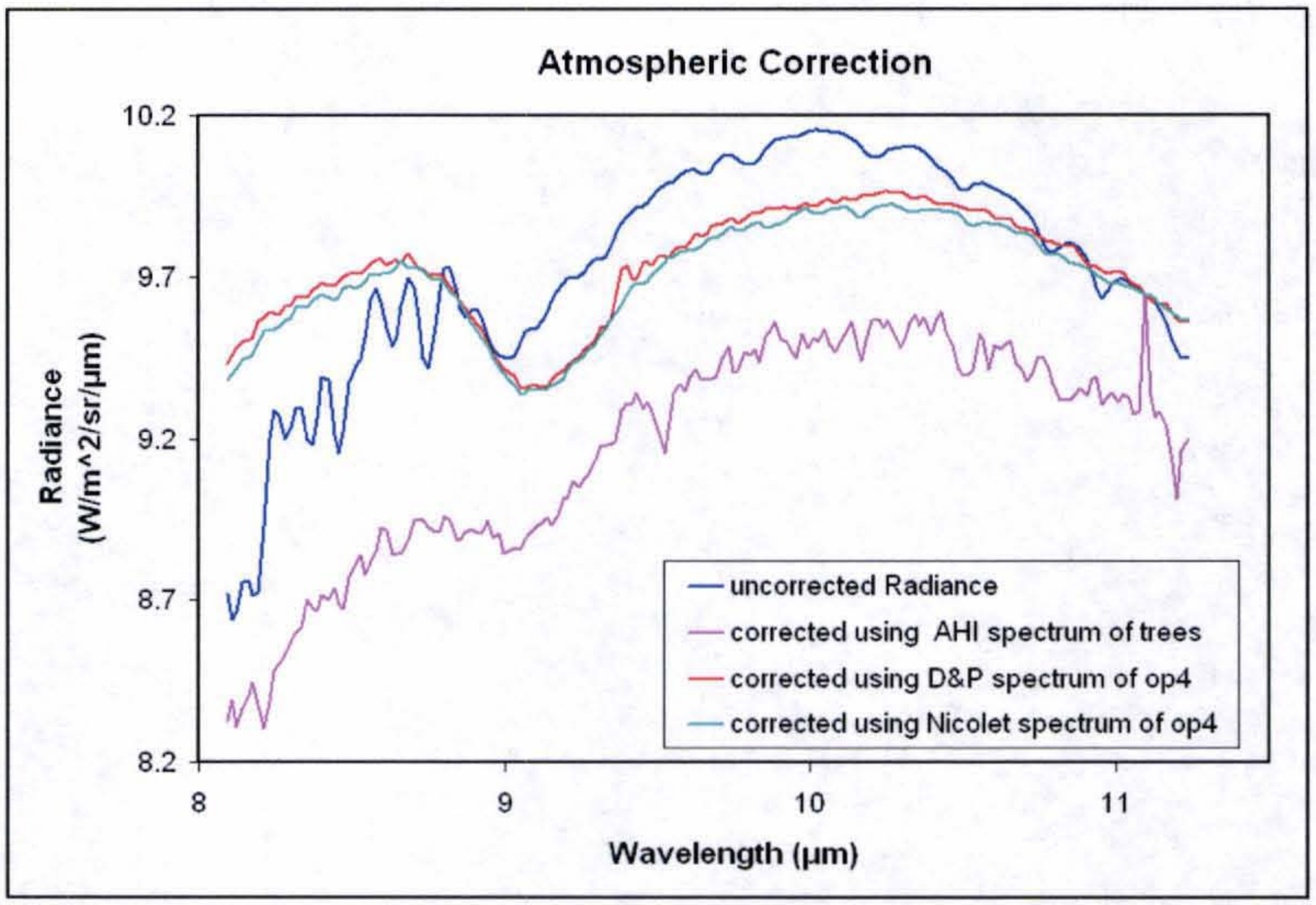

Figure 25. This figure shows the effects of the atmospheric correction routine using different reference spectra. Shown are the uncorrected radiance spectrum of run 5 AHI data, three corrected radiance spectra using an averaged tree spectrum from run 5 AHI data, a Nicolet spectrum of the 4-8ka sample, and a D&P spectrum of the 4-8ka surface. The uncorrected spectrum shows lots of structure in the 8-9µm region, which is mostly due to atmospheric water vapor. Using the tree spectrum, though reducing the atmospheric contributions, adds lots of noise throughout the corrected spectrum. Using a Nicolet or D&P spectrum of the 4-8ka flow reduces the atmospheric contribution with minimum addition of noise

References

Abrams, M., et al. (1991), Combined use of visible, reflected infrared, and thermal infrared images for mapping Hawaiian lava flows, *J. Geophys. Res.*, *96*, 475-484.

Alley, R. E. (1996), Algorithm Theoretical Basis Document for Decorrelation Stretch, Jet Propulsion Laboratory, Pasadena, CA.

Armstrong, R. W. (1983), Atlas of Hawaii, in *Atlas of Hawaii*, edited by R. W. Armstrong, p. 63, University of Hawaii Press.

Crisp, J., et al. (1990), Thermal infrared spectral character of Hawaiian basaltic glasses, *J. Geophys. Res.*, *95*, 21657-21669.

Curtiss, B., et al. (1985), Origin, development and chemistry of silica-alumina rock coatings from the semi-arid regions of the island of Hawaii, *Geochimica et Cosmochimica Acta*, *49*, 49-56.

Elvidge, C. (1979), Distribution and formation of desert varnish in Arizona, M.S. thesis, Arizona State University, Tempe, Arizona.

Farr, T. G., and J. G. Adams (1984), Rock coatings in Hawaii, *Geological Society of America Bulletin*, *95*, 1077-1083.

Gillespie, A. R., et al. (1986), Color Enhancement of Highly Correlated Images. I. Decorrelation and HSI Contrast Stretches., *Remote Sensing of Environment*, *20*, 209-235.

Hamilton, V. E., and P. G. Lucey (2005), One Spectrometer, Two Spectra: Complementary Hemispherical Reflectance and Thermal Emission Spectroscopy Using a Single FTIR Instrument., paper presented at Lunar and Planetary Science Conference.

Hook, S. J., and A. B. Kahle (1996), The Micro Fourier Transform Interferometer (FTIR) – A New Field Spectrometer for Acquisition of Infrared Data of Natural Surfaces, *Remote Sensing of Environment*, *56*, 172-181.

Horton, K. A., et al. (1998), Infrared Measurements of Pristine and Disturbed Soils 2. Environmental Effects and Field Data Reduction, *Remote Sensing of Environment*, *64*, 47-52.

Hunt, G. (1980), Electromagnetic radiation: The communication link in remote sensing, in *Remote Sensing in Geology*, edited by B. S. Siegal and A. R. Gillespie, pp. 5-45, John Wiley, New York.

Juvik, J. O., and D. J. Perreira (1973), The Interception of Fog and Cloud Water on Windward Mauna Loa, Hawaii, 11 pp.

Kahle, A. B., et al. (1988), Relative dating of Hawaiian lava flows using multispectral thermal infrared images - A new tool for geologic mapping of young volcanic terranes, *J. Geophys. Res.*, *93*, 15239-15251.

Korb, A. R., et al. (1996), Portable Fourier Transform Infrared Spectroradiometer for Field Measurements of Radiance and Emissivity, *Applied Optics*, *35*, 1679-1692.

Kraft, M. D., et al. (2003), Effects of Pure Silica Coatings on Thermal Emission Spectra of Basaltic Rocks: Considerations for Martian Surface Mineralogy, *Geophys. Res. Lett.*, *30*, PLA 5-1 - PLA 5-4.

Lucey, P. G., et al. (2004), Recent results from AHI: a LWIR hyperspectral imager, paper presented at Imaging Spectrometry IX, SPIE.

Lucey, P. G., et al. (1998), AHI: an airborne long-wave infrared hyperspectral imager, paper presented at Airborne Reconnaissance XXII, SPIE.

Mysen, B. O. (1983), The Solubility mechanisms of Volatiles in silicate melts and their relations to crystal-andesite liquid equilibria, *J. Volcanol. Geotherm. Res.*, *18*, 361-385.

Rubin, M., et al. (1987), Hawaiian radiocarbon dates, in *U. S. Geological Survey Professional Paper, Report: P 1350*, edited by R. W. Decker, et al., pp. 213-242.

Salisbury, J. W., and D. M. D'Aria (1992), Infrared (8–14 μm) remote sensing of soil particle size, *Remote Sensing of Environment*, *42*, 157-165.

Salisbury, J. W., et al. (1994), Thermal-infrared remote sensing and Kirchhoff 's law 1. Laboratory measurements, *J. Geophys. Res.*, *99*, 11,897-811,911.

Salisbury, J. W., and L. S. Walter (1989), Thermal infrared (2.5 - 13.5 μm) spectroscopic remote sensing of igneous rock types on particulate planetary surfaces, *J. Geophys. Res.*, *94*, 9192 - 9202.

Touloukian, Y. S., and D. P. DeWitt (1970), *Thermal Radiative Properties: Metallic Elements and Alloys*, IFI/Plenum, New York.

Winter, M. E., et al. (2004), Calibration of the University of Hawaii's airborne hyperspectral imager, paper presented at Imaging Spectrometry IX, SPIE, Jan 2004.

Wolfe, E. W., and J. Morris (1996), Geologic Map of the Island of Hawaii, USGS.

Wright, T. L. (1971), Chemistry of Kilauea and Mauna Loa lava in space and time, 40 pp.

Young, S. J., et al. (2002), An in-scene method for atmospheric compensation of thermal hyperspectral data, *J. Geophys. Res.*, *107*.